Article

Volcanic trigger of ocean deoxygenation during Cordilleran ice sheet retreat

https://doi.org/10.1038/s41586-022-05267-y

Received: 12 February 2022

Accepted: 23 August 2022

Published online: 2 November 2022

Check for updates

Jianghui Du[1,2]✉, Alan C. Mix[1], Brian A. Haley[1], Christina L. Belanger[3] & Sharon[3]

North Pacific deoxygenation events during the last deglaciation were sustained over millennia by high export productivity, but the triggering mechanisms and their links to deglacial warming remain uncertain[1–3]. Here we find that initial deoxygenation in the North Pacific immediately after the Cordilleran ice sheet (CIS) retreat[4] was associated with increased volcanic ash in seafloor sediments. Timing of volcanic inputs relative to CIS retreat suggests that regional explosive volcanism was initiated by ice unloading[5,6]. We posit that iron fertilization by volcanic ash[7–9] during CIS retreat fuelled ocean productivity in this otherwise iron-limited region, and tipped the marine system towards sustained deoxygenation. We also identify older deoxygenation events linked to CIS retreat over the past approximately 50,000 years (ref. [4]). Our findings suggest that the apparent coupling between the atmosphere, ocean, cryosphere and solid-Earth systems occurs on relatively short timescales and can act as an important driver for ocean biogeochemical change.

Reduction of dissolved oxygen (known as deoxygenation) in the subsurface ocean is underway and projected to worsen if modern warming trends persist[10]. This deoxygenation will have strong impacts on marine ecosystems, especially in regions that have low-oxygen backgrounds, such as the oxygen minimum zones (OMZs) of the North and East Pacific[11]. Identification of the mechanisms that trigger and sustain long-term deoxygenation is problematic in short modern observational records because of interannual-to-decadal variability[10], which provides impetus for study of the mechanism driving past sustained ocean deoxygenation. Among the best known of such occurrences are the deoxygenation events of the Northeast Pacific during the last deglacial warming (19–9 thousand years ago, hereafter ka). These events, sustained for centuries to millennia, provide a well-constrained climate context that allows investigation into the triggers and impacts of deoxygenation[1–3].

The initial causes of deglacial deoxygenation events have been hypothetically linked to high-latitude warming that reduced oxygen solubility and increased metabolic oxygen demand and productivity[1]. However, warming alone is not sufficient to drive the entire water column to deoxygenation[12]. Alternative hypotheses have linked deoxygenation to slowing subsurface circulation, increasing stratification and northward advection of low-oxygen Pacific Equatorial Water[13–15]; however, deglacial circulation probably accelerated in the abyssal Pacific, whereas no marked change of ventilation has been found at the intermediate depths associated with deoxygenation events[16,17]. Another class of hypotheses implicates shelf iron cycling related to sea-level rise as fuel for increased productivity in the iron-limited North Pacific[3,18]. Although productivity and iron feedbacks may have helped to sustain deoxygenation[1,12,19], the initial triggers remain unclear.

Here we document the potential role of solid-Earth processes in triggering the deglacial deoxygenation. The solid Earth is coupled to the atmosphere–ocean system through the intermediary of the cryosphere on glacial–interglacial timescales; loss of ice cover can trigger explosive volcanism[5]. Modern volcanic ash deposition can lead to surface phytoplankton blooms in iron-limited regions, including the subarctic Pacific[7,8]. We thus suggest that deoxygenation events in the Northeast Pacific were triggered by increasing volcanism as the CIS retreated during the deglacial warming.

To test this hypothesis, we generated high-resolution multi-tracer records of sediment oxygenation at two sites in the Gulf of Alaska (GOA), Northeast Pacific. Our study sites lie within the high-nutrient, low-chlorophyll (HNLC) region, in which surface water is nitrate-replete but primary production is iron-limited (Fig. 1, Extended Data Fig. 1 and Methods). The sites are uniquely positioned at the intersection of the volcanically active Pacific 'Ring of Fire', CIS and the North Pacific HNLC and OMZ, and are thus well suited to monitor the interactions between volcanism, the cryosphere and ocean biogeochemistry. Intermediate-depth site EW0408-85JC and co-located IODP Site U1419 (59.6° N, 144.2° W, 682 m water depth) sit in the upper reaches of the modern OMZ and underlies North Pacific Intermediate Water. Abyssal site EW0408-87JC and co-located IODP Site U1418 (58.8° N, 144.5° W, 3,680 m water depth) are at present bathed by relatively well-oxygenated Pacific deep water that is ventilated by Southern Ocean waters[16]. The contrast in oceanographic background at these two sites provides a further constraint on mechanisms driving deoxygenation.

Published highly resolved radiocarbon-based chronologies are updated using the Marine20 calibration curve[4,20,21] (Methods and Extended Data Fig. 2). We measured authigenic enrichment of a suite of established redox-sensitive metals (Re, U, Cd and Mo) in sediments at sample spacing of about 90 and about 225 years for the intermediate-depth and abyssal sites, respectively. The exceptionally high sedimentation rate (10–1,000 cm kyr^{-1}) at both sites[4,20] diminishes the potential for age offsets between authigenic accumulation and the hosting sediments to a few decades to centuries (Methods). The oxygen

[1]College of Earth, Ocean, and Atmospheric Sciences, Oregon State University, Corvallis, OR, USA. [2]Institute of Geochemistry and Petrology, Department of Earth Sciences, ETH Zürich, Zürich, Switzerland. [3]Department of Geology & Geophysics, Texas A&M University, College Station, TX, USA. ✉e-mail: jianghui.du@erdw.ethz.ch

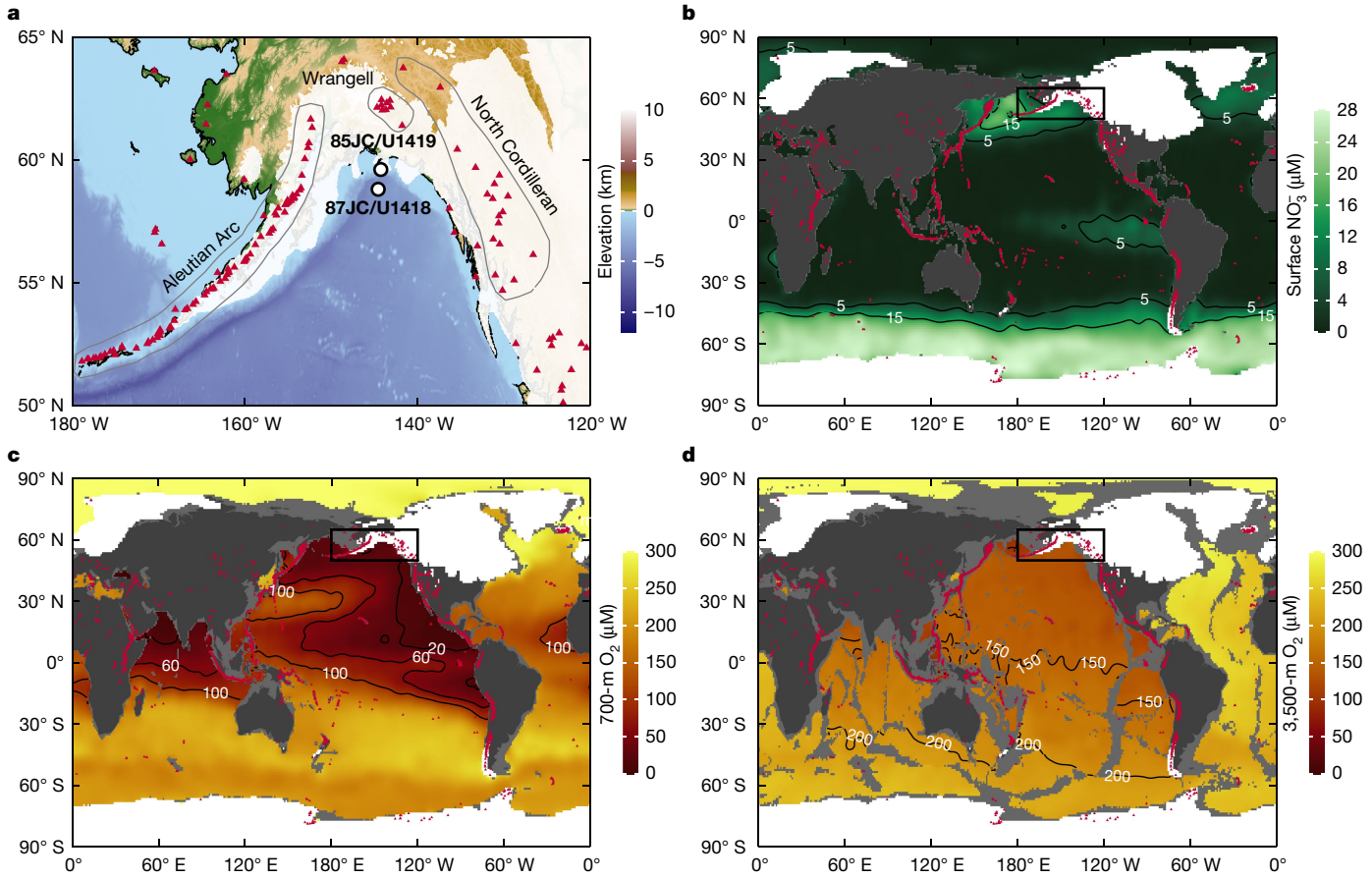

Fig. 1 | Geology and oceanography background. a, Modern land topography and ocean bathymetry in the Northeast Pacific[48]. Circles mark the intermediate-depth site EW0408-85JC/IODP-U1419 and the abyssal site EW0408-87JC/IODP-U1418. **b**, Modern global surface ocean nitrate concentration[49]. **c**,**d**, Modern global ocean oxygen concentration[49] at the 700-m (**c**) and 3,500-m (**d**) depths, respectively. In all panels, red triangles indicate Quaternary volcanoes[50]. The three main regional volcanic fields adjacent to the Northeast Pacific are indicated in **a**. White fields show the LGM ice extent based on regional reconstruction[41] (**a**) and the global ICE-7G model[25] (**b**–**d**). The study region is indicated on the global maps by the black boxes.

thresholds for the enrichment of these metals roughly follow the order of Re, U, Cd and Mo (ref. [22]). As oxygen falls, the accumulations of Re and U increase under suboxic conditions. The enrichments of Cd and Mo often require sulphidic conditions[22]. The use of this metal suite thus allows identification of the various degrees of deoxygenation. The geochemical observations are complemented by the study of the oxygen gradients inferred from benthic foraminifera[12,23]. Faunal species are classified as dysoxic, suboxic and weakly hypoxic-to-oxic, based on literature reports of their modern oxygen thresholds and multivariate ordination analysis with the redox-sensitive metals (Methods).

To reconstruct the local volcanic input, we measured a suite of major and trace elements at the intermediate-depth site, based on total sediment digestion (Methods). Volcanic fractions were quantified by statistical inversion of the geochemical data[24] and independently supported by bulk-sediment radiogenic Nd isotope (ε_{Nd}) evidence for sediment provenance[16] (Extended Data Figs. 3–5). Dispersed ash accounts for a substantial portion of total ash input into marine sediments[24]. Our geochemical sensing thus provides a more complete and continuous record of volcanism than is possible from visual inspection of discrete tephra layers. Because our reconstructions of volcanic fraction, redox and published palaeo-temperature[1,19] are from the same samples, the stratigraphic order of warming, volcanism and deoxygenation that we establish is independent of the age model.

We present a new compilation of regional and global records of well-dated volcanic eruptions based mainly on terrestrial tephra records (Methods), to assess the linkage between our geochemical measures of volcanism from marine sediments and documented eruptions. We calculate the time-varying ratio of the eruptive frequency of glaciated to unglaciated volcanoes[5] normalized to the Last Glacial Maximum (LGM) mean as a proxy for volcanism triggered by ice unloading (Extended Data Fig. 6). We then compare the links between deoxygenation and volcanism to ice sheet dynamics using well-dated records of CIS chronology, including stratigraphically co-registered sedimentological evidence at the study sites[4] and regional surface-exposure dates (Methods). Finally, we analysed the CIS histories reconstructed in two glacial isostatic adjustment (GIA) models, the global ICE-7G (VM7)[25] and the Northern Hemisphere-only LW-6 (ref. [26]), and a high-resolution three-dimensional physical ice sheet model of the CIS based on the Parallel Ice Sheet Model (PISM)[27].

Timing and extent of deoxygenation

The redox-sensitive metals show coherent temporal patterns of deglacial deoxygenation, but with systematic differences in the degree of oxygenation between the intermediate-depth and abyssal sites (Fig. 2). The enrichments of Cd and Mo (Fig. 2e,f) coincide with sediment lamination[3], indicating sulphidic conditions at the intermediate-depth site during the early Bølling–Allerød (15–13.5 ka) and early Holocene (11.7–11 ka) warming intervals[1,3,28]. Enrichments of Re and U (Fig. 2c,d) show that partial deoxygenation was initiated gradually starting around 17 ka, before the severe deoxygenation of Bølling warming, but after the early initial warming at about 21 ka indicated by regional sea-surface

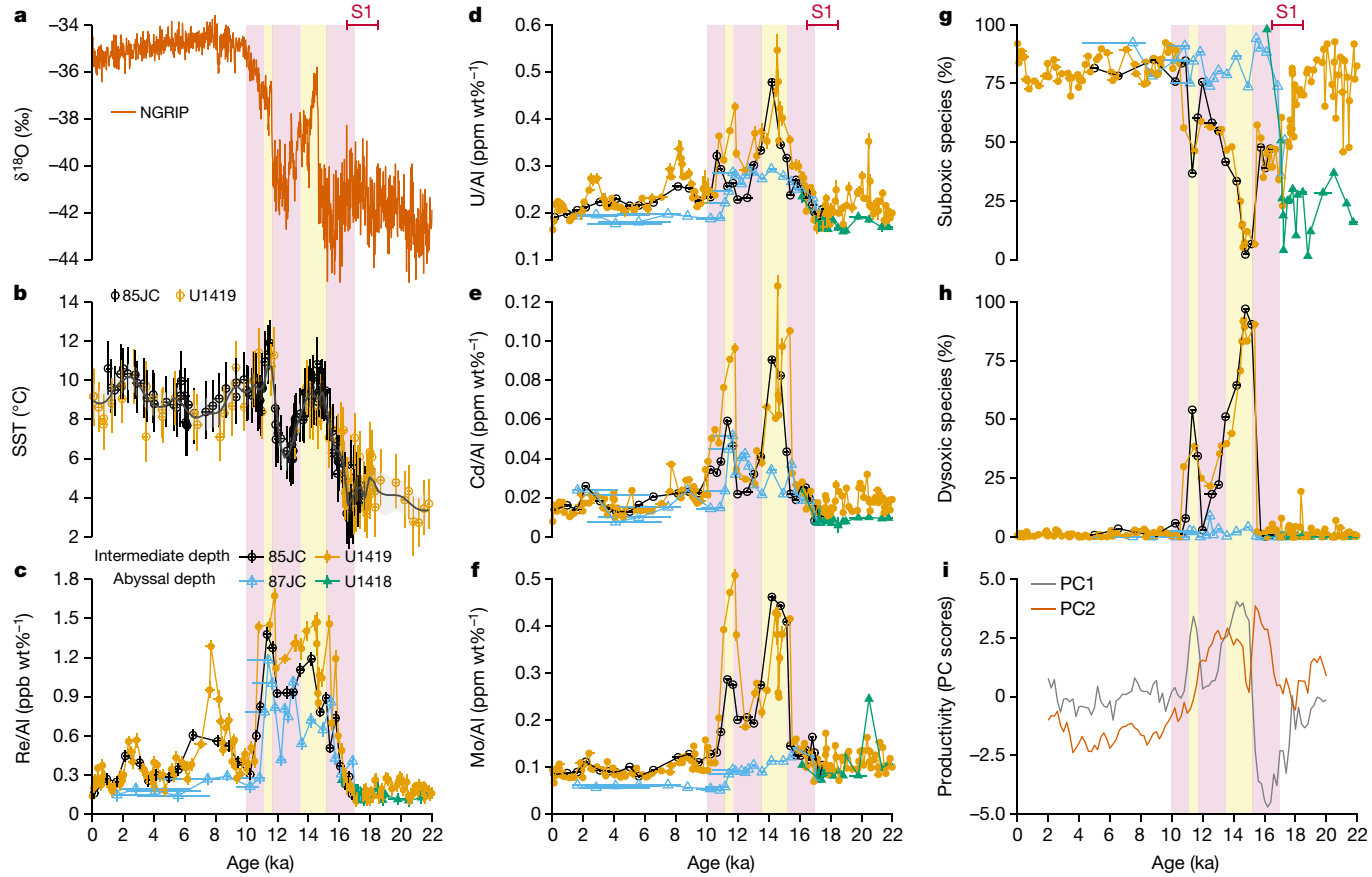

Fig. 2 | Records of deglacial deoxygenation in the Northeast Pacific. **a**, Greenland NGRIP ice core $\delta^{18}O$ on the Antarctic ice core chronology (AICC2012) timescale[51]. **b**, SST at the intermediate-depth site[1,19] (data points with 1σ uncertainty and locally estimated scatterplot smoothing (LOESS) smoothed line with shaded 95% confidence interval (CI)). **c**–**f**, Concentrations of redox-sensitive metals normalized to Al (with 2σ uncertainties) at the intermediate-depth and abyssal sites. **g**,**h**, Abundances of suboxic and dysoxic benthic foraminiferal species[12,23]. The horizontal error bars in **b**–**h** indicate the 95% CIs of age models. The same colour legend applies to **b**–**h**. **i**, Principal components of the productivity proxies from the study sites; PC1 is generally associated with siliceous plankton and PC2 with calcareous plankton (Methods). The yellow bars mark sediment lamination and severe deoxygenation, and the pink bars indicate milder but broader timespans of deoxygenation. The red bars at the top indicate Siku Event 1 (S1)[4].

temperature (SST)[1,19] (Fig. 2a,b). Moreover, Re data show persistent suboxic conditions at the intermediate-depth site throughout the deglaciation (that is, 17–10 ka) (Fig. 2c) and again intermittently during Holocene times, showing a greater duration of partial deoxygenation than previously thought[1,3,28]. By contrast, the lack of Mo enrichment and weak Cd enrichment suggests that sulphidic conditions did not reach the abyssal site during the deglaciation (Fig. 2e,f). Rather, the enrichment of Re and U suggest that suboxic conditions dominated at the abyssal site, similarly to the intermediate-depth site (Fig. 2c,d). The initiation of the deoxygenation is essentially synchronous at both sites.

The oxygen gradients indicated by the redox-sensitive metals are supported by benthic foraminiferal species assemblages[12,23]. Dysoxia-tolerant benthic foraminifera capture the most severe deoxygenation at the intermediate-depth site corresponding to the sulphidic conditions indicated by Mo and Cd (Fig. 2h). Owing to the low-oxygen background at the intermediate-depth site, suboxia-tolerant species are abundant except during severe deoxygenation, when they are replaced by dysoxia-tolerant species (Fig. 2g). The abyssal site lacks dysoxia-tolerant species, whereas increasing abundance of suboxia-tolerant species is consistent with Re and U enrichments in showing the initiation of partial deoxygenation at about 17 ka (Fig. 2g). Redox-sensitive metals and faunal assemblages agree with each other and suggest that the development of deoxygenation are coeval at both sites. This multiproxy and multilocation consistency suggests that age offsets between authigenic metals and the hosting sediments are negligible and that the timing of the deoxygenation events are well captured.

We also find a tight coupling between deoxygenation, phytoplankton community and surface-ocean productivity exported to the seafloor based on several productivity proxies (Extended Data Fig. 7), which we summarize using two principal components (PCs, Fig. 2i and Methods). High PC2 scores indicate an early productivity increase associated with an increase in calcareous plankton[19,28] at about 17 ka corresponding to the initiation of mild deoxygenation. High PC1 scores show a change in the character of productivity that occurred around 15 ka with high diatom export as opal and elevated $\delta^{15}N$ associated with the severe deoxygenation[28]. We suggest that an early (17–15 ka) improvement of the availability of surface-ocean nutrients was exploited by phytoplankton groups that require warming but have modest nutrient requirements. Such an early increase in productivity could have contributed to limited deoxygenation, releasing sediment-sourced nutrients into the water column and making them available to the biota[1]. A subsequently nutrient-replete surface ocean could then host diatom blooms, which are exported more efficiently to the underlying sediments to sustain severe deoxygenation.

The initiation of deoxygenation at about 17 ka is markedly earlier than the onset of sulphidic conditions at about 15 ka. Benthic radiocarbon data indicate that deoxygenation is not associated with slowing of the subsurface circulation[4] (Extended Data Fig. 8b). A sea-surface salinity reconstruction also discounts an association of meltwater and

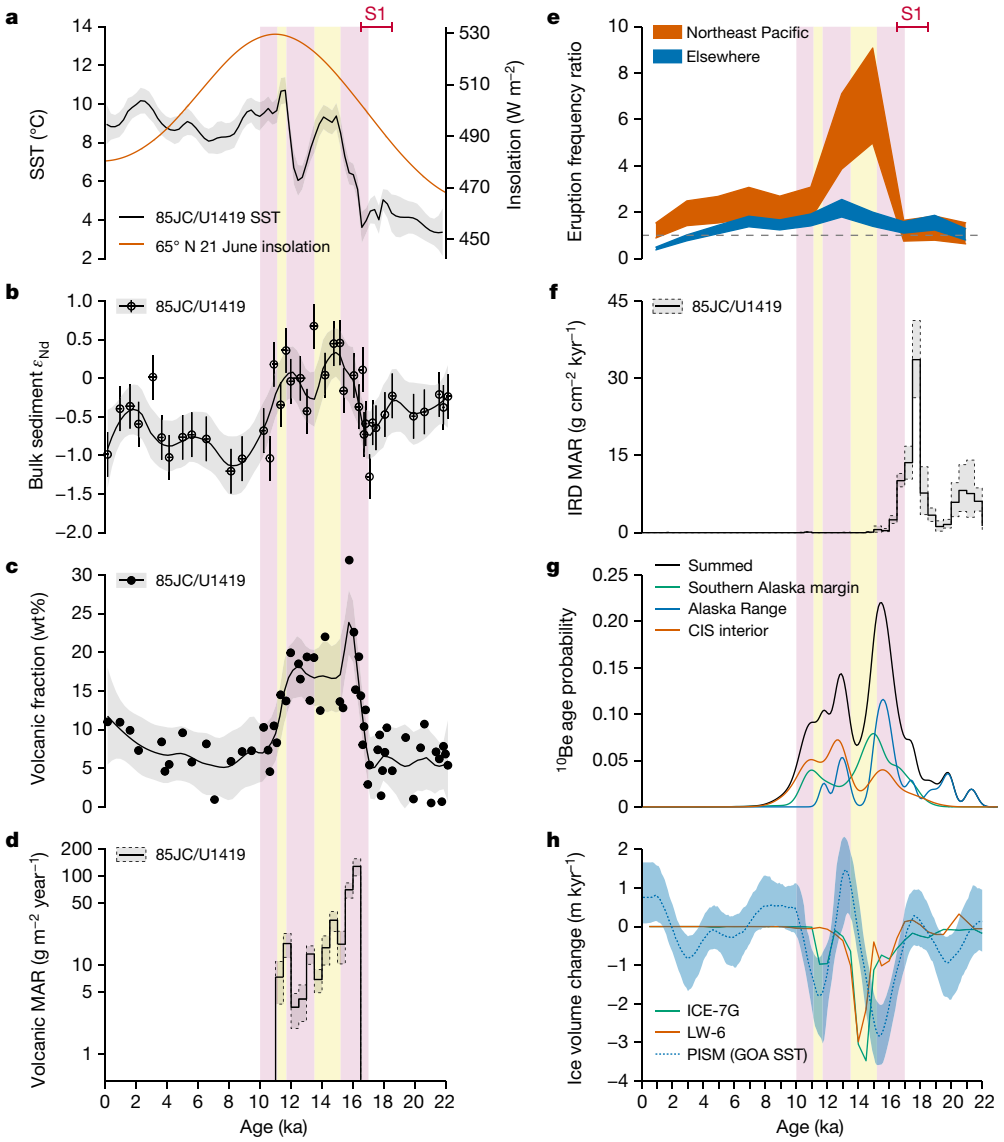

Fig. 3 | Records of deglacial volcanism and ice sheet retreat on the Northeast Pacific margin. a, SST at the intermediate-depth site[1,19] (LOESS smoothed line with shaded 95% CI) and insolation on 21 June at 65° N (ref. [42]). **b**, Bulk sediment ε_{Nd} (points with 2σ uncertainty and LOESS smoothed line with shaded 95% CI; horizontal error bars indicate the 95% CIs of the age model)[16]. **c**, Volcanic ash fraction (LOESS smoothed line with shaded 95% CI). **d**, Volcanic ash MAR in excess of the background (log scale, mean values in line with 1σ range). **e**, Eruption frequency ratios of glaciated volcanoes from the Northeast Pacific margin and glaciated volcanoes from elsewhere in the world. Ribbons indicate interquartile ranges. **f**, IRD MAR (median with 1σ range)[4]. **g**, Probability densities of ^{10}Be age from the northern part of the CIS (north of 55° N). **h**, The rate of CIS volume change, in terms of sea-level equivalent, in the GIA models (LW-6 (ref. [26]) and ICE-7G[25]) and estimated using the sensitivity results of the physical ice sheet model PISM[27] and GOA SST (median with 1σ range).

stratification with deoxygenation[29] (Extended Data Fig. 8c). Deglacial meltwater was probably mostly trapped by the Alaska Coastal Current and transported alongshore to the northwest, as it is today[30] (Extended Data Fig. 1d). Global eustatic sea-level rise is also unlikely to explain the initiation of deoxygenation[3,18], as the relative sea level fell in the northern GOA during the deglaciation because of isostatic rebound and tectonic movement[6,31] (Extended Data Fig. 8d).

The early stages of deoxygenation (17–15 ka) coincided with the minimum strength of the Atlantic Meridional Overturning Circulation (AMOC)[32] (Extended Data Fig. 8e). This timing precludes a hypothesis linking reduction in North Pacific subsurface circulation rates to acceleration of the AMOC[15], adding to growing evidence that North Pacific variability is not a passive responder to the North Atlantic but has its own dynamics[4,29]. Mineral dust transported from Asian deserts to the subpolar North Pacific remained constant during the initiation of deoxygenation, whereas it decreased during the severe deoxygenation[33] (Extended Data Fig. 8f), so we can reject a hypothesis that mineral dust from Asia was a primary driver of productivity and deoxygenation.

Greater volcanism following CIS retreat

At the intermediate-depth site, the ε_{Nd} of lithogenic sediment increased rapidly, starting at about 17 ka, and relatively positive values persisted through the deglaciation (Fig. 3b). As volcanic materials have higher ε_{Nd} (approximately +6 to +10)[34] than regional terrigenous sediments (about −2)[35], more positive values of ε_{Nd} indicate greater volcanic contributions concurrent with the initiation and development of deoxygenation.

Statistical inversion of a broader suite of geochemical data further shows that the volcanic fractions in sediments are dominated by dispersed rhyolitic ash probably sourced from the eastern Aleutian Arc and/or Wrangell Volcanic Field[36] (Fig. 1a and Extended Data Fig. 5).

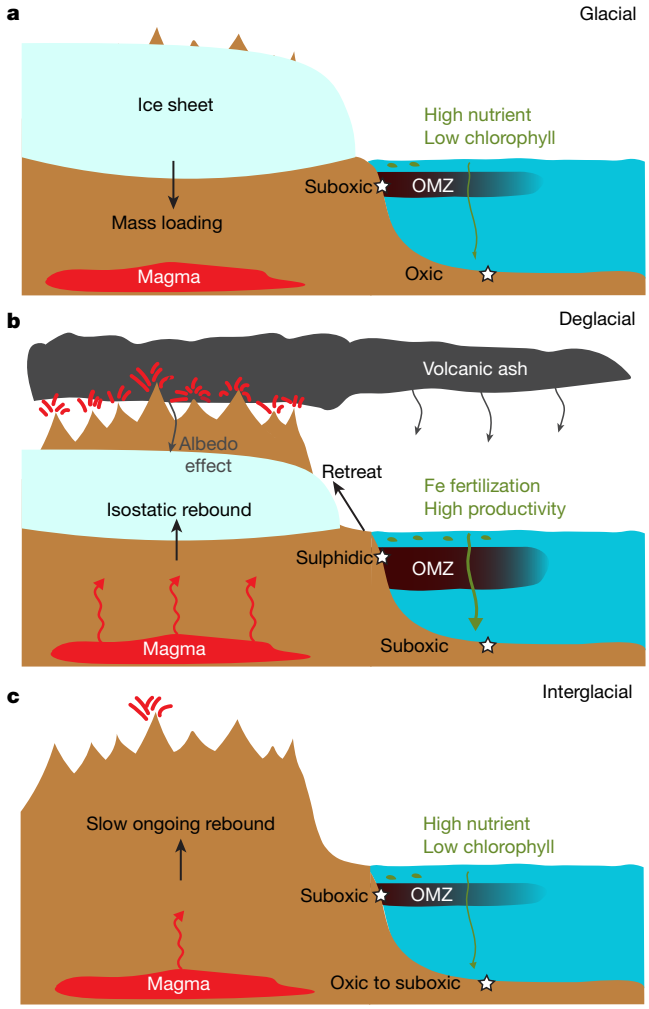

Fig. 4 | Proposed links between ice sheet retreat, volcanism and deoxygenation in the Northeast Pacific. a, The glacial state, with strong mass loading by the ice sheet. Volcanism is depressed. Seafloor oxygenation is similar or slightly better than today and surface productivity is similar or slightly weaker than today[12]. **b**, The deglacial state, with increasing volcanism because of ice sheet retreat, which triggered high productivity and seafloor deoxygenation at both sites. The OMZ probably expanded but probably did not reach the abyssal site. The albedo effect of volcanic ash probably accelerated ice retreat. **c**, The interglacial state, after ice sheet retreat, volcanism becomes weaker. Surface productivity and seafloor oxygenation return to baseline conditions typical of the modern subpolar HNLC North Pacific. The stars mark the intermediate-depth and abyssal sites.

The volcanic ash fraction exceeded background levels at about 17 ka (Fig. 3c) and reached peak values at the beginning (about 16 ka and about 12 ka) of the severe deoxygenation intervals. We calculate the excess volcanic ash mass accumulation rate (MAR) to be about 5–100 g m^{-2} $year^{-1}$ (Fig. 3d) and find that it was comparable with or exceeded the highest atmospheric mineral dust fluxes in the modern ocean[37]. Given that volcanic ash has similar iron solubility to mineral dust[9], such elevated volcanic ash flux during the deglacial interval could have relieved iron limitation and fuelled biological production in the Northeast Pacific.

Increasing deglacial volcanism on the Northeast Pacific margin is also supported by our new compilation of regional and global explosive volcanism. We find that previously glaciated volcanoes in the study region experienced a roughly sixfold increase in activity during the deglaciation relative to the LGM, substantially more than the apparent approximately twofold increase in other glaciated volcanoes from elsewhere in the world (Fig. 3e and Extended Data Fig. 6). The timing of increased volcanism based on the eruption frequency ratio (binned in 2-kyr intervals) is consistent with the high-resolution geochemical record of dispersed ash at the intermediate-depth site. Assuming that terrestrial deposition of tephra can only be preserved after the ice cover was gone, enhanced deglacial volcanism could have occurred even earlier than our terrestrial compilation indicates.

A mechanism often used to explain the increase in volcanism during glacial retreat links ice-mass unloading to reduced crustal pressure and stress, and their influence on magma production and storage[5,38]. Our records indicate that regional volcanism began to increase at around 17 ka, soon after the CIS started to disintegrate. Ice-rafted debris (IRD) at the intermediate-depth site shows that the last major discharge event, Siku Event 1, occurred 18–17 ka (Fig. 3f), after which the bulk of the CIS permanently retreated away from the southern Alaska margin[4]. Terrestrial ^{10}Be exposure dating shows that CIS retreat was underway 19–17 ka on the southern Alaska margin[39], and glacial retreat in the Alaska Range began 21–18 ka, with accelerating pace 17–16 ka (ref. [40]) (Fig. 3g). Radiocarbon-based chronologies[41] document an early deglaciation of the Aleutian Arc (19–17 ka) and a later (15–12 ka) rapid ice loss in the Aleutian and Wrangell volcanic regions (Extended Data Fig. 9a).

Two GIA-based models, ICE-7G[25] and LW-6 (ref. [26]), estimate that most of the CIS mass loss happened 15–13 ka (Fig. 3h). In ICE-7G, ice removal first started 19–17 ka in the northwestern part of the CIS covering the Aleutian and Wrangell regions, as indicated by the radiocarbon chronology (Extended Data Fig. 9), consistent with our geochemical inference that these regions were the probable initial source of increasing volcanism. In LW-6, the earliest CIS deglaciation started 17–15 ka (Fig. 3h). This later date probably results from the model domain of LW-6 excluding the northwestern part of the CIS[26].

In the dynamic ice sheet model PISM[27], notable CIS retreat could have started well before 17 ka, depending on which surface-temperature forcing is applied (Extended Data Fig. 10). Sensitivity experiments under various temperature forcings show high sensitivity of ice loss to local warming (−1.2 ± 0.2 m of sea-level equivalent per °C) with a short time-lag (360 ± 213 year). Given this sensitivity, we predicted the CIS volume change when the GOA SST is applied as forcing. A regional warming trend starting as early as around 21 ka predicts a much greater CIS mass loss in the interval 21–17 ka and 17–15 ka (Fig. 3a,h) than suggested by the GIA-based models, which have limited local sea-level data constraints, particularly from the northwestern side of the CIS. The local SST-based prediction of early ice loss agrees well with the ^{10}Be-constrained CIS chronology (Fig. 3g).

Thus volcanism increased rapidly (around 17 ka) with little time-lag (<4 kyr) following the beginning of CIS unloading (starting as early as around 21 ka), consistent with the detailed case studies of Mount Edgecumbe in southeast Alaska[6] and modelling of the responses of magma chambers to ice unloading[38].

A coupled system

Our results establish close links between surface warming, ice sheet retreat, volcanism, marine productivity and ocean deoxygenation during the last deglaciation on the Northeast Pacific margin (Fig. 4). These linkages imply much tighter coupling of the atmosphere, ocean, cryosphere and solid-Earth systems, on shorter timescales than previously thought.

Increasing summer insolation[42] may have initiated the observed regional warming and ice sheet retreat early in the deglacial sequence around 21 ka (Fig. 3a). If ice unloading induced greater volcanic activity, extensive volcanic ash may in turn have accelerated ice sheet melting through the albedo effects on ice ablation zones[43], yielding further unloading and volcanism. Greater volcanic ash input to the surface ocean, regardless of the transport mechanism (airfall, water or sea-ice transported), would have constituted an increased flux of iron and other

nutrients sufficient to stimulate phytoplankton productivity about 17 ka. With sufficient deoxygenation at the seafloor, iron and nutrient release from reducing sediments delivered to the upper-ocean biota by vertical mixing would have fuelled further productivity and sustained deoxygenation around 15 ka (ref. [1]). Diagenetic mobilization of sedimentary iron in the severe deoxygenation intervals is evidenced by anomalously low palaeo-magnetic intensity at the intermediate-depth site[20,44]. Modern ocean studies have documented that local marginal sources of sedimentary iron can be transported through the subsurface and intermediate water circulation on basinal scales throughout the subpolar North Pacific, stimulating productivity and deoxygenation in the far field[45]. This coupled Earth system thus provides a mechanism to explain the onset and long duration of deglacial deoxygenation events found across the North Pacific at sites that have low-oxygen backgrounds[1,46] (Fig. 1c). Our results thus give impetus to the creation of coupled system models with interactive cryosphere and solid-Earth components to simulate ocean biogeochemical changes on orbital and millennial timescales.

To assess whether such events are unique to major deglaciation or happened frequently in the past, we examined longer records from the same sites and found redox-sensitive metal and benthic faunal evidence for brief deoxygenation events associated with earlier glacial retreats documented in IRD records[4] back to about 50 ka (Fig. 5). These older deoxygenation events typically lasted a few centuries. Such transient events suggest a high sensitivity of ocean oxygenation to perturbations to the coupled system on the Northeast Pacific margin.

Do the solid Earth to ocean biogeochemistry linkages that we identify here also apply to the future? Much of the Cordilleran ice is gone, limiting the power of deglaciation to trigger volcanism, but the remaining ice on the high-elevation stratovolcanoes and other mountainous regions of the Northeast Pacific margin is still substantial and melting is accelerating today[47]. Moreover, modern global warming is putting this region in a precarious near-hypoxic state[10], such that even a modest increase in export productivity fuelled by volcanic iron input could amplify thermal deoxygenation. It is an open question whether increased volcanism might follow from future ice losses, and if so, whether it would suffice to cross deoxygenation thresholds as it did during the deglaciation or whether future deoxygenation will be strong enough to trigger sustaining feedback mechanisms. Nevertheless, the linkages we have identified in the past suggest that the coupling between solid Earth and marine biogeochemical processes can operate relatively quickly and tipping-point behaviours exist that can sustain deoxygenation for millennia, a potential concern for the future.

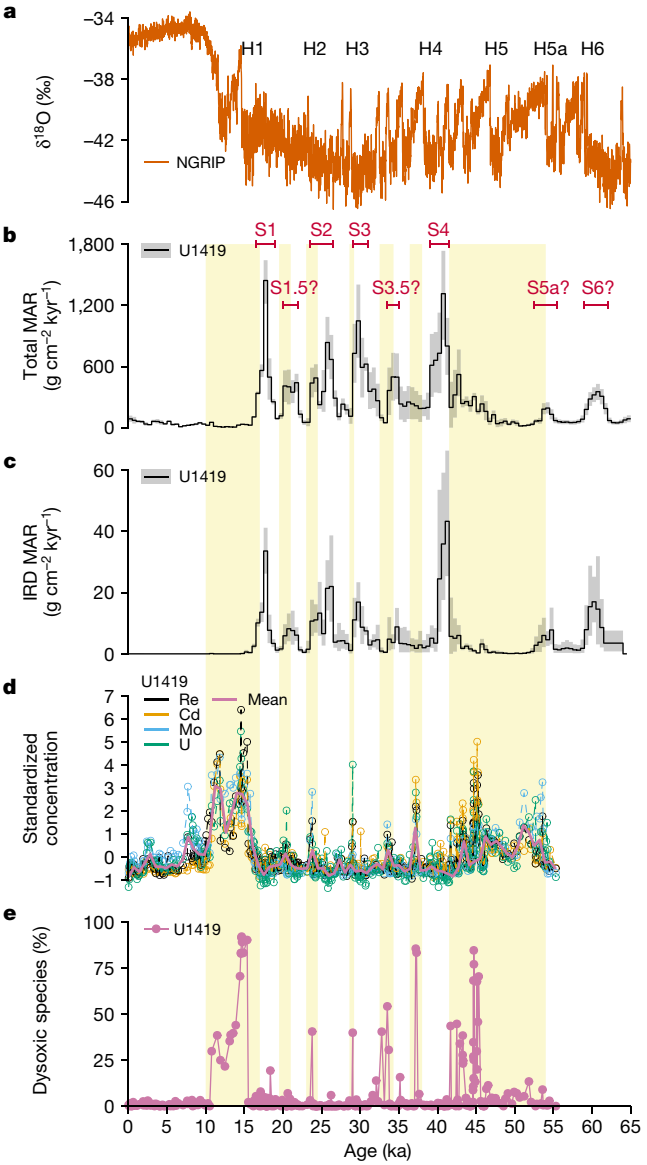

Fig. 5 | Records of ice sheet retreat and deoxygenation on the Northeast Pacific margin in the past 50 kyr. a, Greenland NGRIP ice core $\delta^{18}O$ on the AICC2012 timescale[51]. The Heinrich stadials are labelled. **b**,**c**, Total sediment and IRD MAR (median with 1σ range)[4]. The red bars indicate Siku events[4]. **d**, Standardized concentrations (z scores, means removed) of redox-sensitive metals. The thin, coloured dashed lines represent individual metals. The thick pink line indicates LOESS smoothing running through all metals. **e**, Abundance of dysoxic benthic foraminiferal species. The yellow bars mark the deoxygenation events. The age model and MAR before about 45 ka are beyond the limit of precise radiocarbon dating and are thus uncertain[4].

Online content

Any methods, additional references, Nature Research reporting summaries, source data, extended data, supplementary information, acknowledgements, peer review information; details of author contributions and competing interests; and statements of data and code availability are available at https://doi.org/10.1038/s41586-022-05267-y.

1. Praetorius, S. K. et al. North Pacific deglacial hypoxic events linked to abrupt ocean warming. *Nature* **527**, 362–366 (2015).
2. Crusius, J., Pedersen, T. F., Kienast, S., Keigwin, L. & Labeyrie, L. Influence of northwest Pacific productivity on North Pacific Intermediate Water oxygen concentrations during the Bølling-Ållerød interval (14.7–12.9 ka). *Geology* **32**, 633–636 (2004).
3. Davies, M. H. et al. The deglacial transition on the southeastern Alaska Margin: meltwater input, sea level rise, marine productivity, and sedimentary anoxia. *Paleoceanography* **26**, PA2223 (2011).
4. Walczak, M. H. et al. Phasing of millennial-scale climate variability in the Pacific and Atlantic Oceans. *Science* **370**, 716–720 (2020).
5. Huybers, P. & Langmuir, C. Feedback between deglaciation, volcanism, and atmospheric CO_2. *Earth Planet. Sci. Lett.* **286**, 479–491 (2009).
6. Praetorius, S. et al. Interaction between climate, volcanism, and isostatic rebound in Southeast Alaska during the last deglaciation. *Earth Planet. Sci. Lett.* **452**, 79–89 (2016).
7. Hamme, R. C. Volcanic ash fuels anomalous plankton bloom in subarctic northeast Pacific. *Geophys. Res. Lett.* **37**, L19604 (2010).
8. Browning, T. J. et al. Strong responses of Southern Ocean phytoplankton communities to volcanic ash. *Geophys. Res. Lett.* **41**, 2014GL059364 (2014).
9. Olgun, N. Surface ocean iron fertilization: the role of airborne volcanic ash from subduction zone and hot spot volcanoes and related iron fluxes into the Pacific Ocean. *Glob. Biogeochem. Cycles* **25**, GB4001 (2011).
10. Schmidtko, S., Stramma, L. & Visbeck, M. Decline in global oceanic oxygen content during the past five decades. *Nature* **542**, 335–339 (2017).
11. Levin, L. A. Manifestation, drivers, and emergence of open ocean deoxygenation. *Annu. Rev. Mar. Sci.* **10**, 229–260 (2018).
12. Belanger, C. L., Sharon, Du, J., Payne, C. R. & Mix, A. C. North Pacific deep-sea ecosystem responses reflect post-glacial switch to pulsed export productivity, deoxygenation, and destratification. *Deep Sea Res. Part I Oceanogr. Res. Pap.* **164**, 103341 (2020).
13. Hendy, I. L. & Pedersen, T. F. Is pore water oxygen content decoupled from productivity on the California Margin? Trace element results from Ocean Drilling Program Hole 1017E, San Lucia slope, California. *Paleoceanography* **20**, PA4026 (2005).
14. Lam, P. J. et al. Transient stratification as the cause of the North Pacific productivity spike during deglaciation. *Nat. Geosci.* **6**, 622–626 (2013).

15. Schmittner, A., Galbraith, E. D., Hostetler, S. W., Pedersen, T. F. & Zhang, R. Large fluctuations of dissolved oxygen in the Indian and Pacific oceans during Dansgaard-Oeschger oscillations caused by variations of North Atlantic Deep Water subduction. *Paleoceanography* **22**, PA3207 (2007).
16. Du, J., Haley, B. A., Mix, A. C., Walczak, M. H. & Praetorius, S. K. Flushing of the deep Pacific Ocean and the deglacial rise of atmospheric CO_2 concentrations. *Nat. Geosci.* **11**, 749–755 (2018).
17. Davies-Walczak, M. et al. Late Glacial to Holocene radiocarbon constraints on North Pacific Intermediate Water ventilation and deglacial atmospheric CO_2 sources. *Earth Planet. Sci. Lett.* **397**, 57–66 (2014).
18. Mix, A. C. et al. in *Mechanisms of Global Climate Change at Millennial Time Scales* (eds Clark, P. U., Webb, R. S. & Keigwin, L. D.) 127–148 (American Geophysical Union, 1999).
19. Romero, O. E., LeVay, L. J., McClymont, E. L., Müller, J. & Cowan, E. A. Orbital and suborbital-scale variations of productivity and sea surface conditions in the Gulf of Alaska during the past 54,000 years: impact of iron fertilization by icebergs and meltwater. *Paleoceanogr. Paleoclimatol.* **37**, e2021PA004385 (2022).
20. Velle, J. H. et al. High resolution inclination records from the Gulf of Alaska, IODP Expedition 341 Sites U1418 and U1419. *Geophys. J. Int.* **229**, 345–358 (2022).
21. Heaton, T. J. et al. Marine20—the marine radiocarbon age calibration curve (0–55,000 cal BP). *Radiocarbon* **62**, 779–820 (2020).
22. Morford, J. L. & Emerson, S. The geochemistry of redox sensitive trace metals in sediments. *Geochim. Cosmochim. Acta* **63**, 1735–1750 (1999).
23. Sharon, Belanger, C., Du, J. & Mix, A. Reconstructing paleo-oxygenation for the last 54,000 years in the Gulf of Alaska using cross-validated benthic foraminiferal and geochemical records. *Paleoceanogr. Paleoclimatol.* **36**, e2020PA003986 (2021).
24. Scudder, R. P. Geochemical approaches to the quantification of dispersed volcanic ash in marine sediment. *Prog. Earth Planet. Sci.* **3**, 1 (2016).
25. Roy, K. & Peltier, W. R. Relative sea level in the Western Mediterranean basin: a regional test of the ICE-7G_NA (VM7) model and a constraint on late Holocene Antarctic deglaciation. *Quat. Sci. Rev.* **183**, 76–87 (2018).
26. Lambeck, K., Purcell, A. & Zhao, S. The North American Late Wisconsin ice sheet and mantle viscosity from glacial rebound analyses. *Quat. Sci. Rev.* **158**, 172–210 (2017).
27. Seguinot, J., Rogozhina, I., Stroeven, A. P., Margold, M. & Kleman, J. Numerical simulations of the Cordilleran ice sheet through the last glacial cycle. *Cryosphere* **10**, 639–664 (2016).
28. Addison, J. A. et al. Productivity and sedimentary $\delta^{15}N$ variability for the last 17,000 years along the northern Gulf of Alaska continental slope. *Paleoceanography* **27**, PA1206 (2012).
29. Praetorius, S. K. et al. The role of Northeast Pacific meltwater events in deglacial climate change. *Sci. Adv.* **6**, eaay2915 (2020).
30. Weingartner, T. J., Danielson, S. L. & Royer, T. C. Freshwater variability and predictability in the Alaska Coastal Current. *Deep Sea Res. Part II Top. Stud. Oceanogr.* **52**, 169–191 (2005).
31. Shugar, D. H. et al. Post-glacial sea-level change along the Pacific coast of North America. *Quat. Sci. Rev.* **97**, 170–192 (2014).
32. Ng, H. C. et al. Coherent deglacial changes in western Atlantic Ocean circulation. *Nat. Commun.* **9**, 2947 (2018).
33. Serno, S. et al. Eolian dust input to the Subarctic North Pacific. *Earth Planet. Sci. Lett.* **387**, 252–263 (2014).
34. Du, J., Haley, B. A. & Mix, A. C. Neodymium isotopes in authigenic phases, bottom waters and detrital sediments in the Gulf of Alaska and their implications for paleo-circulation reconstruction. *Geochim. Cosmochim. Acta* **193**, 14–35 (2016).
35. Farmer, G. L., Ayuso, R. & Plafker, G. A Coast Mountains provenance for the Valdez and Orca groups, southern Alaska, based on Nd, Sr, and Pb isotopic evidence. *Earth Planet. Sci. Lett.* **116**, 9–21 (1993).
36. Preece, S. J., Westgate, J. A., Stemper, B. A. & Péwé, T. L. Tephrochronology of late Cenozoic loess at Fairbanks, central Alaska. *GSA Bull.* **111**, 71–90 (1999).
37. Jickells, T. D. et al. Global iron connections between desert dust, ocean biogeochemistry, and climate. *Science* **308**, 67–71 (2005).
38. Wilson, A. M. & Russell, J. K. Glacial pumping of a magma-charged lithosphere: a model for glaciovolcanic causality in magmatic arcs. *Earth Planet. Sci. Lett.* **548**, 116500 (2020).
39. Lesnek, A. J., Briner, J. P., Lindqvist, C., Baichtal, J. F. & Heaton, T. H. Deglaciation of the Pacific coastal corridor directly preceded the human colonization of the Americas. *Sci. Adv.* **4**, eaar5040 (2018).
40. Tulenko, J. P., Briner, J. P., Young, N. E. & Schaefer, J. M. The last deglaciation of Alaska and a new benchmark ^{10}Be moraine chronology from the western Alaska Range. *Quat. Sci. Rev.* **287**, 107549 (2022).
41. Dalton, A. S. et al. An updated radiocarbon-based ice margin chronology for the last deglaciation of the North American Ice Sheet Complex. *Quat. Sci. Rev.* **234**, 106223 (2020).
42. Laskar, J. et al. A long-term numerical solution for the insolation quantities of the Earth. *Astron. Astrophys.* **428**, 261–285 (2004).
43. Muschitiello, F., Pausata, F. S. R., Lea, J. M., Mair, D. W. F. & Wohlfarth, B. Enhanced ice sheet melting driven by volcanic eruptions during the last deglaciation. *Nat. Commun.* **8**, 1020 (2017).
44. Walczak, M. H. et al. A 17,000 yr paleomagnetic secular variation record from the southeast Alaskan margin: regional and global correlations. *Earth Planet. Sci. Lett.* **473**, 177–189 (2017).
45. Nishioka, J. et al. Subpolar marginal seas fuel the North Pacific through the intermediate water at the termination of the global ocean circulation. *Proc. Natl Acad. Sci.* **117**, 12665–12673 (2020).
46. Jaccard, S. L. & Galbraith, E. D. Large climate-driven changes of oceanic oxygen concentrations during the last deglaciation. *Nat. Geosci.* **5**, 151–156 (2012).
47. Ciracì, E., Velicogna, I. & Swenson, S. Continuity of the mass loss of the world's glaciers and ice caps from the GRACE and GRACE Follow-On Missions. *Geophys. Res. Lett.* **47**, e2019GL086926 (2020).
48. *ETOPO1 1 arc-minute global relief model* (National Geophysical Data Center, 2009); https://doi.org/10.7289/V5C8276M.
49. Boyer, T. P. et al. World Ocean Database 2018 (Technical ed. Mishonov, A. V.) NOAA Atlas NESDIS 87 (2018).
50. Global Volcanism Program, 2013. Volcanoes of the World, v. 4.8.7 (12 March 2020). Venzke, E. (ed.). Smithsonian Institution. https://doi.org/10.5479/si.GVP.VOTW4-2013 (2013).
51. Veres, D. et al. The Antarctic ice core chronology (AICC2012): an optimized multi-parameter and multi-site dating approach for the last 120 thousand years. *Clim. Past* **9**, 1733–1748 (2013).

Methods

Modern biogeochemistry

The modern offshore GOA is part of the HNLC region of the subpolar North Pacific, where moderately high surface primary production leads to incomplete use of macronutrients such as nitrate because of iron limitation[52] (Extended Data Fig. 1a–c). By contrast, the southern Alaska coastal water is a highly productive ecosystem that is iron replete but nitrate limited[53]. These two ecological regimes are separated by the shelf break and the two study sites, 85JC/U1419 on the upper slope and 87JC/U1418 on the abyssal plain, both lie within the HNLC region (Extended Data Fig. 1a).

Removal of coastal sources of Fe on the shelf is a plausible reason for low surface Fe concentrations in the HNLC GOA[53–55] (Extended Data Fig. 1b). Near the coast, glacial meltwater delivers Fe dominantly in particulate forms, which is rapidly removed within the inner and middle shelf, trapped by the Alaska Coastal Current[56]. The fate of glacial meltwater is seen in the distribution of surface salinity during the summer season (Extended Data Fig. 1d). The Alaska Coastal Current traps the meltwater and transports it alongshore to the north and west, rather than offshore[30]. Through shelf-cycling, particulate Fe sustains a relatively uniform concentration of dissolved Fe of a few nanomolars in the surface waters on the shelf, but the concentration decreases quickly approaching the shelf break[55] (Extended Data Fig. 1b). This creates a clear biogeochemical boundary between the iron-replete coast/shelf waters and iron-limited HNLC open ocean. Limited offshore transport of shelf-sourced Fe mainly happens by means of two pathways. First, mesoscale eddies impinging on the shelf can deliver shelf waters to the open ocean sporadically[57]. Second, through mixing, shelf-sourced Fe can enter the subsurface or even intermediate waters, which are more capable of long-distance transport, but this requires diffusive upwelling to finally reach the surface of the HNLC regions[45,53,58].

Low atmospheric Fe deposition is another reason for low surface Fe concentration in the GOA. Low dissolved Al concentration (<1 nM) in surface waters seaward of the shelf break in the GOA is an indication of low atmospheric input to the HNLC region[59]. Prevailing westerly winds dictate that the main mineral dust source to the subpolar North Pacific is the Asian continent, with decreasing deposition rate eastward[33]. Despite this, glacial mineral dust is considered a main source of Fe to the HNLC region, as shelf Fe cannot directly reach the open ocean[60].

Fertilization by volcanic ash has also been observed in the modern HNLC subpolar North Pacific[7,61]. Using an average modern mineral dust flux of 1–2 g m^{-2} $year^{-1}$ (ref. [33]), the total mineral dust flux into the subpolar North Pacific (north of 45° N, total area 1.02×10^{13} m^2) is $10–20 \times 10^{15}$ g kyr^{-1}. In comparison, the long-term average of volcanic ash deposition into this region from surrounding subduction arcs (including Kuril, Kamchatka, Aleutian and Alaska) is estimated to be $29–44 \times 10^{15}$ g kyr^{-1} (ref. [9]). Given similar soluble Fe content[9], this implies a comparable or greater Fe source from volcanic ash than mineral dust in this region, on timescales averaged over millennia or longer.

Age models

The age model of the intermediate-depth site was built on 255 foraminiferal ^{14}C dates in the past 55 kyr (ref. [4]). The 85JC ^{14}C data were mapped onto the CCSF-B depth scale of U1419 using gamma-ray-attenuation bulk density (GRA) and magnetic susceptibility (MS) (Extended Data Fig. 2). We update the depth conversion in ref. [4] to improve the alignment of records. To test the robustness of this alignment, we deviate from our chosen depth conversion and compute the resulting root mean square error (RMSE) misfits of GRA and MS between the two sites. The RMSEs of GRA and MS are normalized by scaling to their respective ranges and summed given equal weights. The results show that deviation of more than 1 cm will increase the misfits of GRA and MS, proving that our alignment is optimal. The surface reservoir ages of samples that have paired benthic–planktic ^{14}C dates were estimated using a vertical advection–diffusion box model[4], producing a transient time series of ΔR that averages to 120 ± 220 years on the Marine20 timescale. This average value was then applied to the planktic dates that have no benthic pairs. Benthic dates were calibrated using a fixed ΔR of 860 ± 330 years. Beyond 45 ka, ^{14}C measurements have large errors and, to extend the age model, the IRD record of U1419 was tuned to the North Atlantic IRD stack assuming a Pacific lead of 1,400 years based on the time-lag analysis after 45 ka (ref. [4]).

The age model of the abyssal site is anchored by 38 planktic ^{14}C dates in the past 45 kyr (ref. [20]). The 87JC ^{14}C data were mapped onto the CCSF-B depth scale of U1418 using MS[20]. The robustness of the alignment is tested as described for the intermediate-depth site and the results similarly show that our alignment is optimal (Extended Data Fig. 2). Surface reservoir ages were estimated following the result at the intermediate-depth site.

The final Bayesian age models at both sites were produced using Bchron[62]. We refer to refs. [4,20] for details of the age model reconstruction. During the deglaciation (19–9 ka), the 1σ age model uncertainty is 52 years (median; interquartile range is 47–61 years) at the intermediate-depth site and 53 years (median; interquartile range is 34–87 years) at the abyssal site. Between 19 and 55 ka, the 1σ age model uncertainty is 151 years (median; interquartile range is 117–217 years) at the intermediate-depth site.

Geochemical measurements

Bulk sediment samples were digested in a CEM MARS 6 microwave using HCl-HNO_3-HF. Major and trace element concentrations were measured using inductively coupled plasma atomic emission spectroscopy and quadrupole inductively coupled plasma mass spectrometry, respectively, in the W.M. Keck Collaboratory for Plasma Spectrometry of Oregon State University following established procedures[34,63]. Internal standards were used to correct instrumental drifts for the trace metals. Long-term (over 3 years) reproducibility was typically about 2% and always <10%, monitored by repeated digestion of an in-house marine sediment standard. Further quality control was done by repeated digestion of the sediment reference material PACS-2 and U.S. Geological Survey rock reference materials AGV-1, BHVO-1 and BHVO-2, which agree well with the literature results[23,34].

Redox-sensitive metals

Redox zonation and remobilization in marine sediments can potentially cause depth, and thus age, offsets between the location of preserved metal enrichment and the original sediment–water interface (SWI) when the initial enrichment happened[22]. To rule out such offsets, we use several redox-sensitive metals, which should be affected differentially by redox zonation and remobilization[64]. We further compare the metal proxies with benthic faunal proxies, which are not affected by such offsets[12,23]. The result that the timings of deoxygenation are the same indicated by different metals and benthic faunas confirms that zonation and remobilization are not important at the study sites. Offsets in age are minimized by high sedimentation rates at both sites, which vary from 10 to 1,000 cm kyr^{-1} in the past 55 kyr and are among the highest reported at similar water depths[4,20]. Previous studies have shown that Re enrichment is around 1 cm offset from the SWI in suboxic and sulphidic sediments, whereas the Mo enrichment is about 0.2 cm offset from the SWI in sulphidic sediments[65]. Such depth offsets correspond to <100-year age offsets at our study sites. High sedimentation rates not only reduce age offset owing to zonation but also prevent remobilization by reducing oxygen exposure time[64]. Rhenium is probably the most sensitive to reoxidation[64], but the strong correlation to other redox metals and the benthic faunas rules out remobilization as an important process at the study sites. Moreover, enrichment of these metals in sediment can happen owing to non-redox-related processes, for example, being carried by Fe–Mn oxides and biogenic materials to

sediments[22]. The use of several metals together with the benthic faunas thus helps minimize such potential biases.

On the basis of the age models, our deglacial (19–9-ka) redox-sensitive metal sample spacing is 90 years (median; interquartile range is 53–151 years) at the intermediate-depth site and 225 years (median; interquartile range is 73–360 years) at the abyssal site. Between 19 and 55 ka, the sample spacing is 112 years (median; interquartile range is 55–200 years) at the intermediate-depth site. Considering the high sampling resolutions, low age model uncertainties and small age offsets, we argue that the redox-sensitive metals can constrain the timing of deoxygenation events to about 100 years at the study sites during the deglaciation and a few centuries during the glacial period.

Benthic foraminifera assemblages

Benthic foraminifera data have been published previously, in which species were classified as dysoxic (O_2 < 0.5 ml l^{-1}), suboxic (0.5–1 ml l^{-1}) and weakly hypoxic-to-oxic (>1 ml l^{-1}) based on literature values of oxygen thresholds and multivariate ordination analysis[12,23]. The dysoxic species dominate under the sulphidic conditions of Mo and Cd enrichment, the suboxic species are prevalent under the mildly reducing condition of Re and U enrichment, whereas the weakly hypoxic-to-oxic species represent the low-oxygen background that is not sufficient to cause authigenic metal enrichment.

SSTs

Published SSTs reconstructed using $U^{K'}_{37}$ at the intermediate-depth site 85JC[1] and U1419 (ref. [19]) are here placed on the unified and updated Marine20-based age model[4,21]. The deglacial $U^{K'}_{37}$ records from the two sites are offset following a relationship of $U^{K'}_{37}$ (85JC) = 0.94 × $U^{K'}_{37}$ (U1419) − 0.01 (r = 0.9, $P \ll 0.05$), probably reflecting inter-laboratory offsets. We corrected the published U1419 record to be consistent with that of 85JC and converted $U^{K'}_{37}$ to SST using the calibration program BAYSPLINE[66]. The analytical $U^{K'}_{37}$ offset of 0.03 (1σ = 0.01) between 85JC and U1419 is equivalent to a SST difference of 0.75 °C (1σ = 0.19 °C) using this calibration, which is smaller than the 1.35-°C (1σ) uncertainty of the calibration itself.

Productivity proxies

Ocean and sedimentary processes can potentially cause productivity proxies to not accurately record palaeo-productivity signals, including poor preservation, overprinting of other environmental factors and differing responses of phytoplankton communities[67,68]. We thus adopt a multiproxy approach to provide a more complete picture of productivity change at the study sites during the deglaciation (Extended Data Fig. 7).

High $CaCO_3$ concentrations at the intermediate-depth site are found during the mild deoxygenation intervals, but not the severe deoxygenation intervals (Extended Data Fig. 7a). Sediment Sr/Al ratios (Extended Data Fig. 7b) are correlated to $CaCO_3$ concentrations and thus can be used as a proxy for $CaCO_3$ in the study region. It shows that the patterns of $CaCO_3$ variations at the intermediate-depth and abyssal sites are similar, with the productivity increase beginning at about 17 ka. The correlation of $CaCO_3$ concentration with coccolith counts (Extended Data Fig. 7c) suggests that the increase in productivity during the mild deoxygenation intervals were partly driven by calcareous plankton. Sediment $CaCO_3$ may be affected by dissolution. A previous study found evidence of enhanced dissolution at the intermediate-depth site during the severe deoxygenation intervals but not during the mild deoxygenation intervals[69]. Carbonate dissolution is expected to be stronger at the abyssal site and thus the increase in calcareous productivity indicated here is probably underestimated.

High total organic carbon (TOC) and biogenic opal concentrations at the intermediate-depth site indicate high productivity during the severe deoxygenation intervals (Extended Data Fig. 7d,e). However, during the onset of deoxygenation at 17–15 ka, TOC and opal may not record the moderate productivity increase because of poor preservation, dilution by lithogenic sediments or because diatoms require nutrient-replete conditions, which were probably not prevalent until the productivity–deoxygenation feedback is fully established in the severe deoxygenation intervals.

The bulk sediment organic matter $\delta^{15}N$ at the intermediate-depth site was corrected for terrestrial organic input to indicate marine organic matter $\delta^{15}N$ (ref. [28]) (Extended Data Fig. 7f). High $\delta^{15}N$ indicates greater surface-ocean nutrient use or sediment denitrification during the severe deoxygenation intervals, and the initial increase at around 17 ka is consistent with the early increase in productivity corresponding to the early onset of deoxygenation indicated by Re.

Sediment Ba/Al ratios at the intermediate-depth site are correlated to opal concentrations, reflecting the high productivity during the severe deoxygenation intervals (Extended Data Fig. 7g). However, barite is undersaturated in the water column at intermediate depths in the North Pacific[70] and barite dissolution in sediments may happen at suboxic conditions and strongly so under sulphidic conditions[71]. Biogenic Ba to carbon ratios also increase with water depth[72]. Thus Ba/Al ratios at the intermediate-depth site are lower than at the abyssal site in the subpolar North Pacific[67], and probably only record the very high diatom-dominated productivity during the severe deoxygenation intervals but not the moderate increase in productivity during the onset of deoxygenation. The abyssal site Ba/Al ratio is probably less affected by undersaturation and diagenesis, and captures the increase of productivity at around 17 ka, as well as throughout the deoxygenation, consistent with the increase in suboxic benthic foraminiferal species.

Increases in the abundance of benthic foraminiferal species linked to organic detritus indicates the initial increase of productivity 17–15 ka (Extended Data Fig. 7h). The benthic species we show are *Islandiella norcrossi* at the intermediate-depth site and *Elphidium batialis* at the abyssal site. *Islandiella norcrossi* thrives under highly productive waters near seasonal sea ice margin[73]. However, it is a shallow-water species that is normally not found in deep-sea sediments. *Elphidium batialis* is phytophagous[74] and only found at the abyssal site. Both species became the most abundant taxon at their respective sites 17–15 ka but are outcompeted when more severe deoxygenation prevails.

We summarized the productivity proxies using principal component analysis[75,76]. The coccolith counts are excluded in principal component analysis because of low sample resolution. PC1 (34%) and PC2 (30%) account for most of the total variance in the proxy data (Fig. 2i). PC1 has high loadings on opal, TOC and Ba/Al ratio from the intermediate-depth site, with its high scores indicating diatom-driven high productivity during severe deoxygenation. PC2 has high loadings on $CaCO_3$ and Sr/Al ratio from both sites, with its high scores indicating the moderately high productivity increase during the mild deoxygenation intervals, probably driven by calcareous phytoplankton growth.

Geochemical provenance analysis

The GOA is surrounded by three major volcanic fields: the Aleutian Arc (AA), the Wrangell Volcanic Field (WVF) and the North Cordilleran Volcanic Field (NCVF), as well as many other small volcanic centres (Fig. 1a). To estimate the volcanic fraction in sediments at the intermediate-depth site, we first identify the volcanic endmembers. Because volcanic materials from different volcanoes often overlap in geochemistry, and the erupted materials of the same volcano often evolve geochemically over time, we do not seek to fingerprint the individual volcanoes that produced the volcanic materials found at our sites but instead we seek endmembers that are clearly defined by geochemistry[24].

We derive geochemical endmembers by analysing the Alaska Volcano Observatory (AVO)[77] and the GEOROC databases (https://georoc.eu/georoc/new-start.asp). The AVO is a comprehensive collection of Quaternary volcanic samples in the State of Alaska, USA. The AA and the WVF are represented in this database. The GEOROC is a collection of global igneous rock samples. We used the samples from Yukon and British Columbia, Canada, in the precompiled North American Cordillera

(Cenozoic to Quaternary) sub-database[78], including samples from the NCVF. We extracted major and trace element data of volcanic materials, including glass (tephra) and whole-rock analyses. We performed cluster analysis using the following set of elements: SiO_2, TiO_2, Al_2O_3, FeO_T, MnO, MgO, CaO, Na_2O, K_2O, Rb, Ba, Sr, La, Ce, Nd, Eu, Tb, Ho, Yb, Zr and Nb, as a reasonable compromise to maximize both the number of samples and the number of elements (most samples only have limited numbers of the elements reported). In total, 2,273 unique samples were included. We performed hierarchical cluster analysis using the complete-linkage method[79] with the Aitchison distance[80] (equivalent to using the Euclidean distance on isometric logratio-transformed data), which is ideal for compositional data analysis because it resolves the 'closure problem'.

We identified five major volcanic clusters (rare clusters smaller than 2% of the total samples were ignored) and the geochemical distinctions are shown in a total alkali-silica diagram, a rare-earth element (REE) pattern and a trace element spidergram (Extended Data Fig. 3). The clusters are defined as (in order of decreasing size): basalt–andesite–dacite; basalt (tholeiitic); basalt (alkaline); rhyolite (adakite) and rhyolite (typical arc). Although the clusters are not unique to any specific volcanoes, general correspondence does exist: (1) Quaternary tephra samples in Alaska mainly fall into the rhyolite clusters, which are separated into a 'typical arc' cluster and an adakite cluster, with the latter characterized by greater light REE enrichment. These two clusters are commonly known as the type I and type II ashes in Alaska tephrochronology[81,82]. The typical arc cluster mostly originates from the central AA, whereas the adakite cluster mostly comes from the WVF and the Alaska Peninsula (the eastern AA). (2) The basalt–andesite–dacite cluster represents the main volcanic rock and lava series of the AA, although it is common elsewhere too. Some deglacial terrestrial and marine tephra found on the southern Alaska margin belong to this cluster[6,83]. (3) The basalt (alkaline) cluster is mainly found in the NCVF[84], as well as some volcanic centres in the Bering Sea. We calculated the geometric means of each cluster and used them as the final geochemical endmembers of volcanic materials for purposes of linear mixing modelling later.

Next we define the terrigenous endmembers. Provenance studies based on thermochronology[85–87], zircon geochemistry[85] and heavy minerals[88] show that the Pleistocene terrigenous sediments at the intermediate-depth and abyssal sites are mainly delivered by the Bagley-Bering Glacier system, which brings eroded materials from the Cretaceous–Eocene accretionary complex of the Chugach–Prince William terrane[89]. The Chugach–Prince William terrane includes the Valdez and Orca groups, consisting mainly of metasedimentary rocks and minor metabasite rocks, with increasing degree of metamorphism towards the Chugach Metamorphic Complex eastward in the Saint Elias Mountains. These terranes are intruded by the Palaeocene–Eocene Sanak–Baranof plutonic belt.

We compiled published major and trace element data of these terrestrial geological endmembers[90–96]. We calculated the Aitchison distances between the geological endmembers and the Holocene (<10 ka) and Glacial (22–17 ka) sediment samples at the intermediate-depth site (outside the intervals of deglacial deoxygenation) using the following set of elements: TiO_2, Al_2O_3, FeO_T, MnO, MgO, Na_2O, K_2O, La, Ce, Nd, Eu, Tb, Yb and Zr, representing a compromise between maximizing the number of samples and the number of elements included. Potentially biogenic elements in marine sediments (Si, Ca, Ba and Sr) were not included. The Aitchison distance helps to identify the similarity between GOA sediments and the potential terrigenous endmembers.

Previous studies found that the terrigenous sediment provenance on the southern Alaska margin has been stable since the Pleistocene[85–88]. This is borne out by the statistically indistinguishable bulk sediment ε_{Nd} at the intermediate-depth site between the Glacial and Holocene samples (Fig. 3b), suggesting that the geochemical changes during the deglaciation were not driven by changes in terrigenous sediment provenance but instead reflect changes in other lithogenic inputs (that is, volcanic ash). Consistently, the major and trace element data (Extended Data Fig. 4) show that Glacial and Holocene sediments at the intermediate-depth site lie within the geochemical space spanned by the potential terrigenous endmembers and that internal differences between the Glacial and Holocene sediments are negligible when compared with the differences between the GOA sediments and the potential terrigenous endmembers. This finding indicates stability of background terrigenous sediment provenance despite the changes in sedimentation and erosion rates from the LGM to the Holocene[4].

We are interested in the relative partitioning of volcanic and terrigenous sediments. The stability of the terrigenous sediment provenance implies that the terrigenous sediments can be effectively treated as a near-constant mixture, consistent in Holocene and Glacial sediments. Thus we take the compositions of the Holocene and Glacial sediments as heuristic terrigenous endmembers. This approach allows us to partition terrigenous sediments relative to volcanic sediments within reasonable uncertainties without a comprehensive partitioning of the terrigenous provenance (the endmembers of which are less geochemically constrained).

Geochemical data inversion

The distinct geochemistry of volcanic endmembers and the apparent stability of the terrigenous sediment provenance allow us to quantify their contributions to marine sediments at the intermediate-depth site using geochemical inversion[24]. We interpret the inversion results based on the well-established geochemical characterization of volcanic, particularly ash, sources in the Alaska tephrochronology[81,82].

The geochemical provenance analysis at the intermediate-depth site is formulated as the inverse problem of a constrained linear mixing model:

$$\text{Minimise } \|(\mathbf{Ax}-\mathbf{b})/\boldsymbol{\delta}\|_2, \text{ subject to } \Sigma\mathbf{x}=1 \text{ and } \mathbf{x}\geq 0 \qquad (1)$$

Here $\mathbf{A}$ is the matrix consisting of multidimensional elemental concentrations of the endmembers, in which each column is an endmember and each row is an element, $\mathbf{b}$ is the elemental concentrations of a sediment sample and $\mathbf{x}$ is the mixing fractions of the endmembers to be solved, which are non-negative and sum to one. $\boldsymbol{\delta}$ is the weighting vector consisting of the external standard deviations of the elements resulting from repeated digestion and analysis of the reference materials. In total, 26 elements (Al_2O_3, MgO, Na_2O, K_2O, FeO_T, MnO, TiO_2, Cr, Cu, Ni, Zn, all 14 REEs and Zr) were used. Bulk sediment ε_{Nd} was not used in the mixing model but it serves as an independent check on the reconstruction of volcanic fraction.

Elemental concentrations of sediment samples were first normalized to a 100% lithogenic fraction basis. Biogenic (organic matter, carbonate and opal) and lithogenic fractions at the intermediate-depth site were previously measured on selected samples[28]. From these data, we derived a multiple linear regression to estimate the lithogenic fractions using density, Al, Ca and Ba concentrations as predictors ($r^2 = 0.9$, $P \ll 0.05$). Sediments on the southern Alaska margin are predominantly lithogenic[97] and, at the intermediate-depth site, the lithogenic fractions varied little since the LGM (90 ± 3 wt%)[28], making this correction minor. Finally, the results of the inversion give the weight fractions of the volcanic and terrigenous endmembers within lithogenic sediments, which are then converted back to weight fractions within the total sediments. We solved problem (1) using a linear least-squares algorithm with non-negativity constraint[98].

The rhyolite (adakite), rhyolite (typical arc) and basalt (alkaline) endmembers all had their greatest relative abundance during the deglaciation (Extended Data Fig. 5). The dominance of the two rhyolite ash endmembers is consistent with the depositional patterns of ash plumes during modern eruptions[99] and in agreement with the dominance of these two clusters in the Quaternary terrestrial tephrochronology of Alaska[81,82]. The implication is that the eastern portion of the AA and the WVF were more active during the deglaciation. The minor increase in the

basalt (alkaline) endmember may be attributed to greater input from the NCVF or the volcanic centres in the Bering Sea. The lack of correlation between ash abundance and sediment MAR shows that the variation of the ash fraction was not compromised by a dilution effect (Extended Data Fig. 5b). The constancy of the volcanic ash fraction between the LGM and the Holocene, despite changes in sediment MAR, suggests a 'background ash' fraction of roughly 7%. We then calculated the excess volcanic ash fractions and fluxes after removing this background.

Global and regional records of deglacial volcanism

We compiled published global and regional records of volcanic eruptions since the LGM. Our compilation includes the Global Volcanism Program (GVP) database[50], the Bryson et al. radiocarbon database[100], the Watt et al. selected volcanic arc database[101], the Large Magnitude Explosive Volcanic Eruptions (LaMEVE) database[102], the Alaska Volcano Observatory eruption database[77] and other recent studies in Alaska[6,83,103]. The previous global compilation of Huybers and Langmuir[5] was based on Bryson et al. and an older version of the GVP. Our new compilation updated the GVP and also included the LaMEVE and AVO as well as other recent data, which increased the deglacial coverage. We removed duplicates among the databases, standardized the volcano names and added the unique volcano numbers following the GVP convention. This makes the compilation traceable and easier for future extension. In Huybers and Langmuir[5], small-magnitude eruptions (volcanic explosivity index ≤ 2) in the GVP were removed, but we chose to keep all eruptions in our compilation for the sake of consistency, as eruption magnitudes were rarely reported. In total, there are 12,403 events reported since 24 ka. Following Huybers and Langmuir[5], we assigned a standard deviation equal to 10% of the reported age when age errors were not available (excluding historical observations that were assumed to be precisely dated). We recalibrated radiocarbon dates using Bchron[62] with IntCal20 (ref. [104]) whenever raw dates were available.

We identify glaciated volcanoes using the modern ice volume balance following Huybers and Langmuir[5], who assumed that previously glaciated regions probably have less negative ice volume balance today. The modern ice volume balance is calculated using the NCEP/NCAR reanalysis of precipitation and temperature[105], and volcanoes that have a modern ice volume balance >-9 m year^{-1} are considered glaciated, like in Huybers and Langmuir[5]. Eruption events were binned into 2-kyr intervals (Extended Data Fig. 6). Like Huybers and Langmuir[5], we assumed that the temporal sampling biases of eruption events in the glaciated and unglaciated volcano datasets are the same. Thus the eruption frequency ratio of the glaciated volcanoes to the unglaciated ones may remove this bias and can be used as a proxy for glaciation-induced volcanism. Finally, we normalized the eruption frequency ratio relative to the LGM mean ratio (22–24 ka), which diverged from Huybers and Langmuir[5], who chose to normalize to the past 2 kyr. We believe that the LGM normalization is probably a less biased normalizer because, although the numbers of eruption events during the LGM and deglacial are within one order of magnitude (Extended Data Fig. 6), two orders of magnitude more eruptions are recorded in the past 2 kyr. The difference in sampling bias between the LGM and the deglaciation is presumably smaller than between them and the past 2 kyr. Our results thus address the question "Was deglacial volcanism more active than that of the LGM?" rather than the question "Was deglacial volcanism more active than that of the past 2 kyr", as originally investigated by Huybers and Langmuir[5]. Regardless, the choice of normalization will affect the absolute magnitude, but not the relative change, of the eruption frequency ratio. To evaluate the impact of dating uncertainties, binning and ratioing was performed 1,000 times in Monte Carlo simulations, including Gaussian distributions of ages for each eruption event.

^{10}Be exposure dates

We compiled published ^{10}Be exposure dates from the regions that were previously covered by the northern part of the CIS (north of 55° N) surrounding the GOA, including the southern Alaska margin[39,106–108], the Alaska Range[40,109,110] and the interior of the CIS[111,112]. We calculated the weighted average and standard deviation of ^{10}Be age at each sample site. We then computed the probability density of the age distribution at each of the three regions using kernel density estimation[113], giving equal weight to each sample site within the same region. Finally, we summed the probability density of all three regions, giving equal weight to each region.

The CIS in PISM sensitivity experiments

We analysed the sensitivity of the CIS volume to the surface temperature forcing in the PISM experiments performed by Seguinot et al.[27,114] (https://zenodo.org/record/3606536). Lacking regional surface temperature records suitable for CIS experiments, Seguinot et al. applied hypothetical surface temperature forcing scaled to other temperature records, including the Greenland Ice Core Project (GRIP)[115] and the North Greenland Ice Core Project (NGRIP)[116] ice core records, the Antarctic EPICA[117] and VOSTOK[118] ice core records and SST records from the California margin sites ODP 1012 and ODP 1020 (ref. [119]). The temperature records were scaled to anomalies that have average glacial (22–32 ka) temperature 6–7 °C lower than today[27] (Extended Data Fig. 10a). We identified the deglacial time-lag of the ice volume response to temperature forcing by computing the cross-correlation of the 0–26-ka part of the ice volume and temperature time series (except for the sensitivity experiment using the ODP 1012 SST forcing, which has a much earlier deglaciation, and we thus used the 6–32-ka part of the time series) (Extended Data Fig. 10d). The average time-lag is 468 ± 362 years (1σ) when including all eight sensitivity experiments. However, the experiments using the ODP 1012 SST forcing appear to be outliers, as the ice volume response is inconsistent with ice sheet reconstructions[27]. Excluding these outliers, the average time-lag is 360 ± 213 years (1σ). Linear regression between ice volume and lagged temperature gives a sensitivity of an ice loss of 1.2 ± 0.2 (1σ) metres of sea-level equivalent per 1 °C of warming (Extended Data Fig. 10e).

On the basis of the ice volume–temperature relationship in the sensitivity experiments, we estimated the CIS volume response had the GOA SST record been used as the temperature forcing (Extended Data Fig. 10f). The GOA SST record is scaled to have a glacial temperature anomaly of −6 °C, consistent with the sensitivity experiments. We then predict the CIS response to GOA SST forcing using the time-lagged linear regression results from the sensitivity experiments (Extended Data Fig. 10e). We perform 10,000 Monte Carlo samplings to propagate errors, including the errors of the SST calibration and the uncertainties of the time-lag and ice sheet response in the PISM sensitivity experiments (Fig. 3h and Extended Data Fig. 10f).

Data availability

The geochemical datasets generated by this study and the data compilations are publicly available at Zenodo (https://doi.org/10.5281/zenodo.6770650) and Pangea (https://doi.org/10.1594/PANGAEA.947051; https://doi.org/10.1594/PANGAEA.947052). Source data are provided with this paper.

Code availability

Computer codes used in the study are publicly available (https://doi.org/10.5281/zenodo.6770650).

52. Martin, J. H., Gordon, R. M., Fitzwater, S. & Broenkow, W. W. VERTEX: phytoplankton/iron studies in the Gulf of Alaska. *Deep Sea Res. Part A Oceanogr. Res. Pap.* **36**, 649–680 (1989).
53. Lippiatt, S. M., Lohan, M. C. & Bruland, K. W. The distribution of reactive iron in northern Gulf of Alaska coastal waters. *Mar. Chem.* **121**, 187–199 (2010).
54. Aguilar-Islas, A. M. et al. Temporal variability of reactive iron over the Gulf of Alaska shelf. *Deep Sea Res. Part II Top. Stud. Oceanogr.* **132**, 90–106 (2016).

55. Crusius, J., Schroth, A. W., Resing, J. A., Cullen, J. & Campbell, R. W. Seasonal and spatial variabilities in northern Gulf of Alaska surface water iron concentrations driven by shelf sediment resuspension, glacial meltwater, a Yakutat eddy, and dust. *Glob. Biogeochem. Cycles* **31**, 942–960 (2017).
56. Wu, J. et al. Size-fractionated iron distribution on the northern Gulf of Alaska. *Geophys. Res. Lett.* **36**, L11606 (2009).
57. Brown, M. T., Lippiatt, S. M., Lohan, M. C. & Bruland, K. W. Trace metal distributions within a Sitka eddy in the northern Gulf of Alaska. *Limnol. Oceanogr.* **57**, 503–518 (2012).
58. Lam, P. J. et al. Wintertime phytoplankton bloom in the subarctic Pacific supported by continental margin iron. *Glob. Biogeochem. Cycles* **20**, GB1006 (2006).
59. Brown, M. T., Lippiatt, S. M. & Bruland, K. W. Dissolved aluminum, particulate aluminum, and silicic acid in northern Gulf of Alaska coastal waters: glacial/riverine inputs and extreme reactivity. *Mar. Chem.* **122**, 160–175 (2010).
60. Crusius, J. Dissolved Fe supply to the central Gulf of Alaska is inferred to be derived from Alaskan glacial dust that is not resolved by dust transport models. *J. Geophys. Res. Biogeosci.* **126**, e2021JG006323 (2021).
61. Duggen, S., Croot, P., Schach, U. & Hoffmann, L. Subduction zone volcanic ash can fertilize the surface ocean and stimulate phytoplankton growth: evidence from biogeochemical experiments and satellite data. *Geophys. Res. Lett.* **34**, L01612 (2007).
62. Haslett, J. & Parnell, A. A simple monotone process with application to radiocarbon-dated depth chronologies. *J. R. Stat. Soc. Ser. C Appl. Stat.* **57**, 399–418 (2008).
63. Muratli, J. M., McManus, J., Mix, A. & Chase, Z. Dissolution of fluoride complexes following microwave-assisted hydrofluoric acid digestion of marine sediments. *Talanta* **89**, 195–200 (2012).
64. Crusius, J. & Thomson, J. Comparative behavior of authigenic Re, U, and Mo during reoxidation and subsequent long-term burial in marine sediments. *Geochim. Cosmochim. Acta* **64**, 2233–2242 (2000).
65. Crusius, J., Calvert, S., Pedersen, T. & Sage, D. Rhenium and molybdenum enrichments in sediments as indicators of oxic, suboxic and sulfidic conditions of deposition. *Earth Planet. Sci. Lett.* **145**, 65–78 (1996).
66. Tierney, J. E. & Tingley, M. P. BAYSPLINE: a new calibration for the alkenone paleothermometer. *Paleoceanogr. Paleoclimatol.* **33**, 281–301 (2018).
67. Serno, S. et al. Using the natural spatial pattern of marine productivity in the Subarctic North Pacific to evaluate paleoproductivity proxies. *Paleoceanography* **29**, 2013PA002594 (2014).
68. Lopes, C., Kucera, M. & Mix, A. C. Climate change decouples oceanic primary and export productivity and organic carbon burial. *Proc. Natl Acad. Sci.* **112**, 332–335 (2015).
69. Payne, C. R. & Belanger, C. L. Enhanced carbonate dissolution associated with deglacial dysoxic events in the subpolar North Pacific. *Paleoceanogr. Paleoclimatol.* **36**, e2020PA004206 (2021).
70. Rushdi, A. I., McManus, J. & Collier, R. W. Marine barite and celestite saturation in seawater. *Mar. Chem.* **69**, 19–31 (2000).
71. McManus, J. et al. Geochemistry of barium in marine sediments: implications for its use as a paleoproxy. *Geochim. Cosmochim. Acta* **62**, 3453–3473 (1998).
72. Dymond, J., Suess, E. & Lyle, M. Barium in deep-sea sediment: a geochemical proxy for paleoproductivity. *Paleoceanography* **7**, 163–181 (1992).
73. Seidenkrantz, M.-S. Benthic foraminifera as palaeo sea-ice indicators in the subarctic realm – examples from the Labrador Sea–Baffin Bay region. *Quat. Sci. Rev.* **79**, 135–144 (2013).
74. Fontanier, C. et al. Living (stained) deep-sea foraminifera off Hachinohe (NE Japan, Western Pacific): environmental interplay in oxygen-depleted ecosystems. *J. Foraminifer. Res.* **44**, 281–299 (2014).
75. Lê, S., Josse, J. & Husson, F. FactoMineR: an R package for multivariate analysis. *J. Stat. Softw.* **25**, 1–18 (2008).
76. Josse, J. & Husson, F. missMDA: a package for handling missing values in multivariate data analysis. *J. Stat. Softw.* **70**, 1–31 (2016).
77. Cameron, C. E., Mulliken, K. M., Crass, S. W., Schaefer, J. R. & Wallace, K. L. *Alaska Volcano Observatory geochemical database, version 2* (Alaska Division of Geological & Geophysical Surveys, 2019); https://doi.org/10.14509/30058
78. *GEOROC Compilation: Intraplate Volcanic Rocks* (DIGIS, 2022); https://doi.org/10.25625/RZZ9VM.
79. Templ, M., Filzmoser, P. & Reimann, C. Cluster analysis applied to regional geochemical data: problems and possibilities. *Appl. Geochem.* **23**, 2198–2213 (2008).
80. Egozcue, J. J., Pawlowsky-Glahn, V., Mateu-Figueras, G. & Barceló-Vidal, C. Isometric logratio transformations for compositional data analysis. *Math. Geol.* **35**, 279–300 (2003).
81. Preece, S. J., Westgate, J. A., Froese, D. G., Pearce, N. J. G. & Perkins, W. T. A catalogue of late Cenozoic tephra beds in the Klondike goldfields and adjacent areas, Yukon Territory. *Can. J. Earth Sci.* **48**, 1386–1418 (2011).
82. Westgate, J. A., Perkins, W. T., Fuge, R., Pearce, N. J. G. & Wintle, A. G. Trace-element analysis of volcanic glass shards by laser ablation inductively coupled plasma mass spectrometry: application to tephrochronological studies. *Appl. Geochem.* **9**, 323–335 (1994).
83. Wilcox, P. S. et al. A new set of basaltic tephras from Southeast Alaska represent key stratigraphic markers for the late Pleistocene. *Quat. Res.* **92**, 246–256 (2019).
84. Edwards, B. R. & Russell, J. K. Northern Cordilleran volcanic province: a northern Basin and Range? *Geology* **27**, 243–246 (1999).
85. Huber, B., Bahlburg, H., Berndt, J., Dunkl, I. & Gerdes, A. Provenance of the Surveyor Fan and precursor sediments in the Gulf of Alaska—implications of a combined U-Pb, (U-Th)/He, Hf, and rare earth element study of detrital zircons. *J. Geol.* **126**, 577–600 (2018).
86. Dunn, C. A., Enkelmann, E., Ridgway, K. D. & Allen, W. K. Source to sink evaluation of sediment routing in the Gulf of Alaska and Southeast Alaska: a thermochronometric perspective. *J. Geophys. Res. Earth Surf.* **122**, 711–734 (2017).
87. Bootes, N., Enkelmann, E. & Lease, R. Late Miocene to Pleistocene source to sink record of exhumation and sediment routing in the Gulf of Alaska from detrital zircon fission-track and U-Pb double dating. *Tectonics* **38**, 2703–2726 (2019).
88. Huber, B., Bahlburg, H. & Pfänder, J. A. Single grain heavy mineral provenance of garnet and amphibole in the Surveyor fan and precursor sediments on the Gulf of Alaska abyssal plain — implications for climate-tectonic interactions in the St. Elias orogen. *Sediment. Geol.* **372**, 173–192 (2018).
89. Plafker, G., Moore, J. C. & Winkler, G. R. in *The Geology of Alaska* (eds Plafker, G. & Berg, H. C.) 389–448 (Geological Society of America, 1994).
90. Harris, N. R., Sisson, V. B., Wright, J. E. & Pavlis, T. L. Evidence for Eocene mafic underplating during fore-arc intrusive activity, eastern Chugach Mountains, Alaska. *Geology* **24**, 263–266 (1996).
91. Sisson, V. B. et al. in *Geology of a Transpressional Orogen Developed During Ridge-Trench Interaction Along the North Pacific Margin* (eds. Sisson, V. B., Roeske, S. M. & Pavlis, T. L.) 293–326 (Geological Society of America, 2003).
92. Plafker, G., Nokleberg, W. J. & Lull, J. S. Bedrock geology and tectonic evolution of the Wrangellia, Peninsular, and Chugach Terranes along the Trans-Alaska Crustal Transect in the Chugach Mountains and Southern Copper River Basin, Alaska. *J. Geophys. Res. Solid Earth* **94**, 4255–4295 (1989).
93. Polat, A. et al. Lithological, structural, and geochemical characteristics of the Mesoarchean Târtoq greenstone belt, southern West Greenland, and the Chugach – Prince William accretionary complex, southern Alaska: evidence for uniformitarian plate-tectonic processes. *Can. J. Earth Sci.* **53**, 1336–1371 (2016).
94. Lull, J. S., Plafker, G., Dover, J. H. & Galloway, J. P. Geochemistry and paleotectonic implications of metabasaltic rocks in the Valdez Group, southern Alaska. *US Geol. Surv. Bull.* **1946**, 29–38 (1990).
95. Barker, F., Farmer, G. L., Ayuso, R. A., Plafker, G. & Lull, J. S. The 50 Ma granodiorite of the eastern Gulf of Alaska: melting in an accretionary prism in the forearc. *J. Geophys. Res. Solid Earth* **97**, 6757–6778 (1992).
96. Bruand, E., Gasser, D., Bonnand, P. & Stuewe, K. The petrology and geochemistry of a metabasite belt along the southern margin of Alaska. *Lithos* **127**, 282–297 (2011).
97. Walinsky, S. E. et al. Distribution and composition of organic matter in surface sediments of coastal Southeast Alaska. *Cont. Shelf Res.* **29**, 1565–1579 (2009).
98. Haskell, K. H. & Hanson, R. J. An algorithm for linear least squares problems with equality and nonnegativity constraints. *Math. Program.* **21**, 98–118 (1981).
99. Bolton, M. S. M. et al. Machine learning classifiers for attributing tephra to source volcanoes: an evaluation of methods for Alaska tephras. *J. Quat. Sci.* **35**, 81–92 (2020).
100. Bryson, R. U., Bryson, R. A. & Ruter, A. A calibrated radiocarbon database of late Quaternary volcanic eruptions. *eEarth Discuss.* **1**, 123–134 (2006).
101. Watt, S. F. L., Pyle, D. M. & Mather, T. A. The volcanic response to deglaciation: evidence from glaciated arcs and a reassessment of global eruption records. *Earth Sci. Rev.* **122**, 77–102 (2013).
102. Crosweller, H. S. et al. Global database on large magnitude explosive volcanic eruptions (LaMEVE). *J. Appl. Volcanol.* **1**, 4 (2012).
103. Davies, L. J., Jensen, B. J. L., Froese, D. G. & Wallace, K. L. Late Pleistocene and Holocene tephrostratigraphy of interior Alaska and Yukon: key beds and chronologies over the past 30,000 years. *Quat. Sci. Rev.* **146**, 28–53 (2016).
104. Reimer, P. J. et al. The IntCal20 Northern Hemisphere radiocarbon age calibration curve (0–55 cal kBP). *Radiocarbon* **62**, 725–757 (2020).
105. Kalnay, E. et al. The NCEP/NCAR 40-year reanalysis project. *Bull. Am. Meteorol. Soc.* **77**, 437–472 (1996).
106. Lesnek, A. J., Briner, J. P., Baichtal, J. F. & Lyles, A. S. New constraints on the last deglaciation of the Cordilleran Ice Sheet in coastal Southeast Alaska. *Quat. Res.* **96**, 140–160 (2020).
107. Haeussler, P. J. et al. Late Quaternary deglaciation of Prince William Sound, Alaska. *Quat. Res.* **105**, 115–135 (2022).
108. Walcott, C. K., Briner, J. P., Baichtal, J. F., Lesnek, A. J. & Licciardi, J. M. Cosmogenic ages indicate no MIS 2 refugia in the Alexander Archipelago, Alaska. *Geochronology* **4**, 191–211 (2022).
109. Briner, J. P. et al. The last deglaciation of Alaska. *Cuad. Investig. Geogr.* **43**, 429–448 (2017).
110. Tulenko, J. P., Briner, J. P., Young, N. E. & Schaefer, J. M. Beryllium-10 chronology of early and late Wisconsinan moraines in the Revelation Mountains, Alaska: insights into the forcing of Wisconsinan glaciation in Beringia. *Quat. Sci. Rev.* **197**, 129–141 (2018).
111. Menounos, B. et al. Cordilleran Ice Sheet mass loss preceded climate reversals near the Pleistocene Termination. *Science* **358**, 781–784 (2017).
112. Dulfer, H. E., Margold, M., Engel, Z., Braucher, R. & Team, A. Using ^{10}Be dating to determine when the Cordilleran Ice Sheet stopped flowing over the Canadian Rocky Mountains. *Quat. Res.* **102**, 222–233 (2021).
113. R Core Team. R: a language and environment for statistical computing (R Foundation for Statistical Computing, 2013).
114. Seguinot, J. et al. *Cordilleran ice sheet glacial cycle simulations continuous variables* (Zenodo, 2020); https://doi.org/10.5281/zenodo.3606536
115. Dansgaard, W. et al. Evidence for general instability of past climate from a 250-kyr ice-core record. *Nature* **364**, 218–220 (1993).
116. Andersen, K. K. et al. High-resolution record of Northern Hemisphere climate extending into the last interglacial period. *Nature* **431**, 147–151 (2004).
117. Jouzel, J. et al. Orbital and millennial Antarctic climate variability over the past 800,000 years. *Science* **317**, 793–796 (2007).
118. Petit, J. R. et al. Climate and atmospheric history of the past 420,000 years from the Vostok ice core, Antarctica. *Nature* **399**, 429–436 (1999).
119. Herbert, T. D. et al. Collapse of the California Current during glacial maxima linked to climate change on land. *Science* **293**, 71–76 (2001).
120. Behrenfeld, M. J. & Falkowski, P. G. Photosynthetic rates derived from satellite-based chlorophyll concentration. *Limnol. Oceanogr.* **42**, 1–20 (1997).
121. Roberts, M. V. *The Temporal and Spatial Distribution of Dissolved and Particulate Iron Over the Gulf of Alaska Shelf*. Thesis, Univ. Alaska Fairbanks (2018).
122. Tagliabue, A. et al. A global compilation of dissolved iron measurements: focus on distributions and processes in the Southern Ocean. *Biogeosciences* **9**, 2333–2349 (2012).

123. GEOTRACES Intermediate Data Product Group. *The GEOTRACES Intermediate Data Product 2021 (IDP2021)* (NERC EDS British Oceanographic Data Centre NOC, 2021); https://www.bodc.ac.uk/data/published_data_library/catalogue/10.5285/cf2d9ba9-d51d-3b7c-e053-8486abc0f5fd/
124. Hauri, C. et al. A regional hindcast model simulating ecosystem dynamics, inorganic carbon chemistry, and ocean acidification in the Gulf of Alaska. *Biogeosciences* **17**, 3837–3857 (2020).
125. Garcia, H. E. et al. World Ocean Atlas 2018. Vol. 4: Dissolved Inorganic Nutrients (Phosphate, Nitrate and Nitrate+Nitrite, Silicate) NOAA Atlas NESDIS 84 (Tech. ed. Mishonov, A.) (NOAA, 2019).
126. Zweng, M. M. et al. *World Ocean Atlas 2018. Vol. 2: Salinity* NOAA Atlas NESDIS 82 (Technical ed. Mishonov, A.) (NOAA, 2019).
127. Le Maitre, R. W. et al. *Igneous Rocks: A Classification and Glossary of Terms. Recommendations of the International Union of Geological Sciences Subcommission on the Systematics of Igneous Rocks* (Cambridge Univ. Press, 2002).
128. McDonough, W. F. & Sun, S.-S. The composition of the Earth. *Chem. Geol.* **120**, 223–253 (1995).

Acknowledgements We thank J. Muratli for assistance in geochemical analysis at Oregon State University. Funding for this study was provided by US NSF award 1502754 to A.C.M. and 1801511 to C.L.B. J.D. was supported by the ETH Zurich Postdoctoral Fellowship 19-2 FEL-32. This project has received funding from the European Union's Horizon 2020 research and innovation programme under the Marie Skłodowska-Curie grant agreement 891489. We thank the Oregon State University Marine and Geology Repository and the International Ocean Discovery Program for access to core materials.

Author contributions J.D. and A.C.M. designed this study. J.D. conducted the geochemical analysis and modelling, data compilation and synthesis and led the writing of the manuscript. A.C.M. assisted the overall conceptualization and interpretation of results and contributed substantially to the writing of the manuscript. B.A.H. assisted with the interpretation of geochemical data and writing of the manuscript. C.L.B. and Sharon helped with the faunal–trace metal data comparison and analysis.

Competing interests The authors declare no competing interests.

Additional information

Supplementary information The online version contains supplementary material available at https://doi.org/10.1038/s41586-022-05267-y.

Correspondence and requests for materials should be addressed to Jianghui Du.

Peer review information *Nature* thanks Weiqi Yao and the other, anonymous, reviewer(s) for their contribution to the peer review of this work.

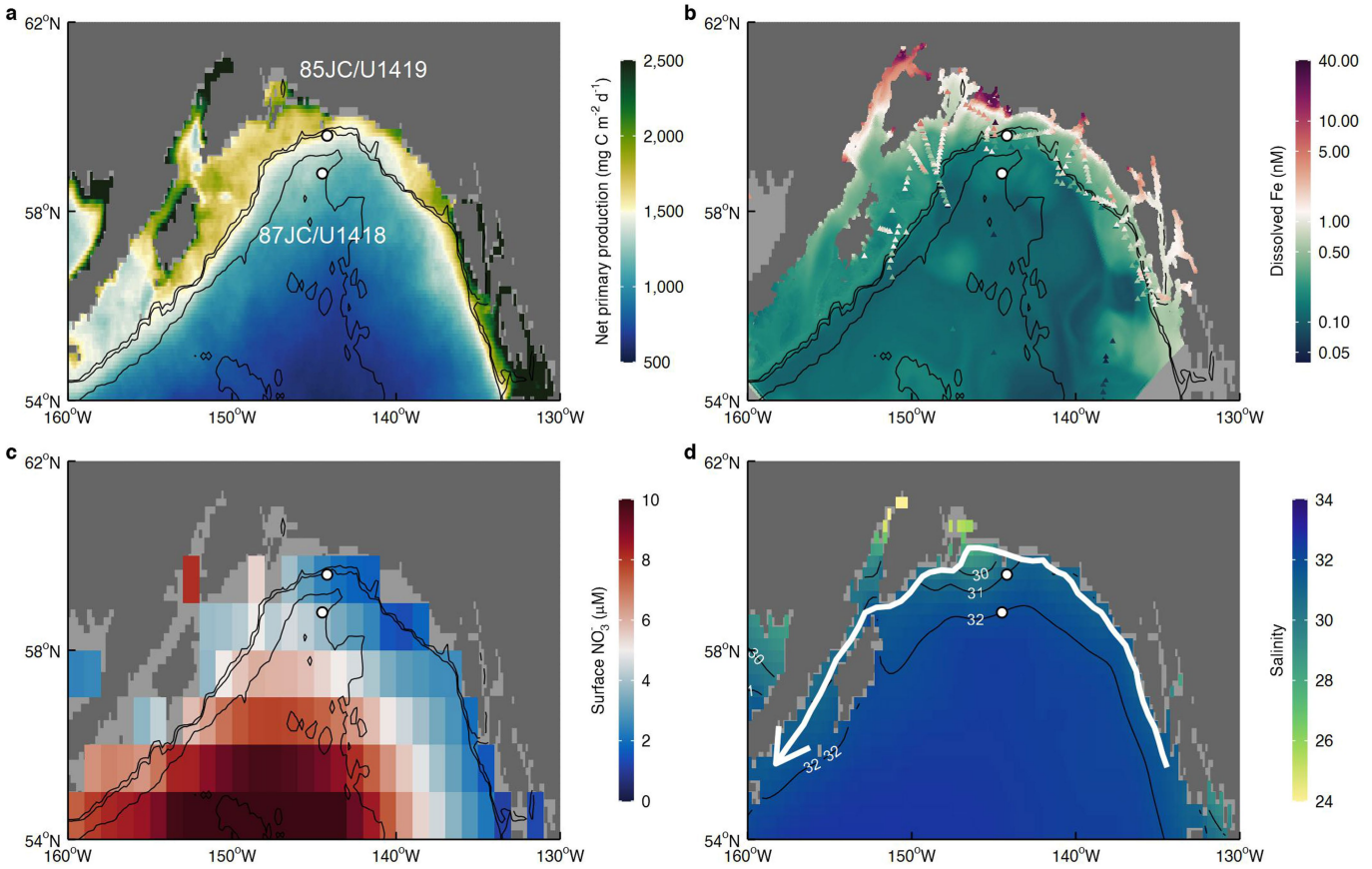

Extended Data Fig. 1 | Modern biogeochemistry of the GOA. a, Net primary production, based on the Vertically Generalized Production Model and the Moderate Resolution Imaging Spectroradiometer satellite results[120], integrated over the euphotic zone and averaged over the spring and summer months (April to September) from 2002 to 2020. **b**, Surface water dissolved Fe concentrations, measured[53–55,121–123] (triangles, averaged over 0–100 m) and from a high-resolution regional hind-cast model[124] (background colour, averaged over 0–100 m and the spring and summer months from 1980 to 2013). The colour bar is in log scale. **c**, Surface NO_3^- climatology (μM, 1-degree grid) from the World Ocean Atlas 2018 (ref. [125]), averaged over 0–100 m and the spring and summer months. **d**, Surface salinity climatology (0.25-degree grid) from the World Ocean Atlas 2018 (ref. [126]), at 0 m and averaged over the summer months. The three black lines in **a**–**c** are the isobaths of 300 m, indicating the depth of the shelf break; 680 m, the depth of site 85JC/U1419; and 3,680 m, the depth of site 87JC/U1418. The three black lines in **d** are the isohalines of 30, 31 and 32. The white arrow in **d** indicates the Alaska Coastal Current.

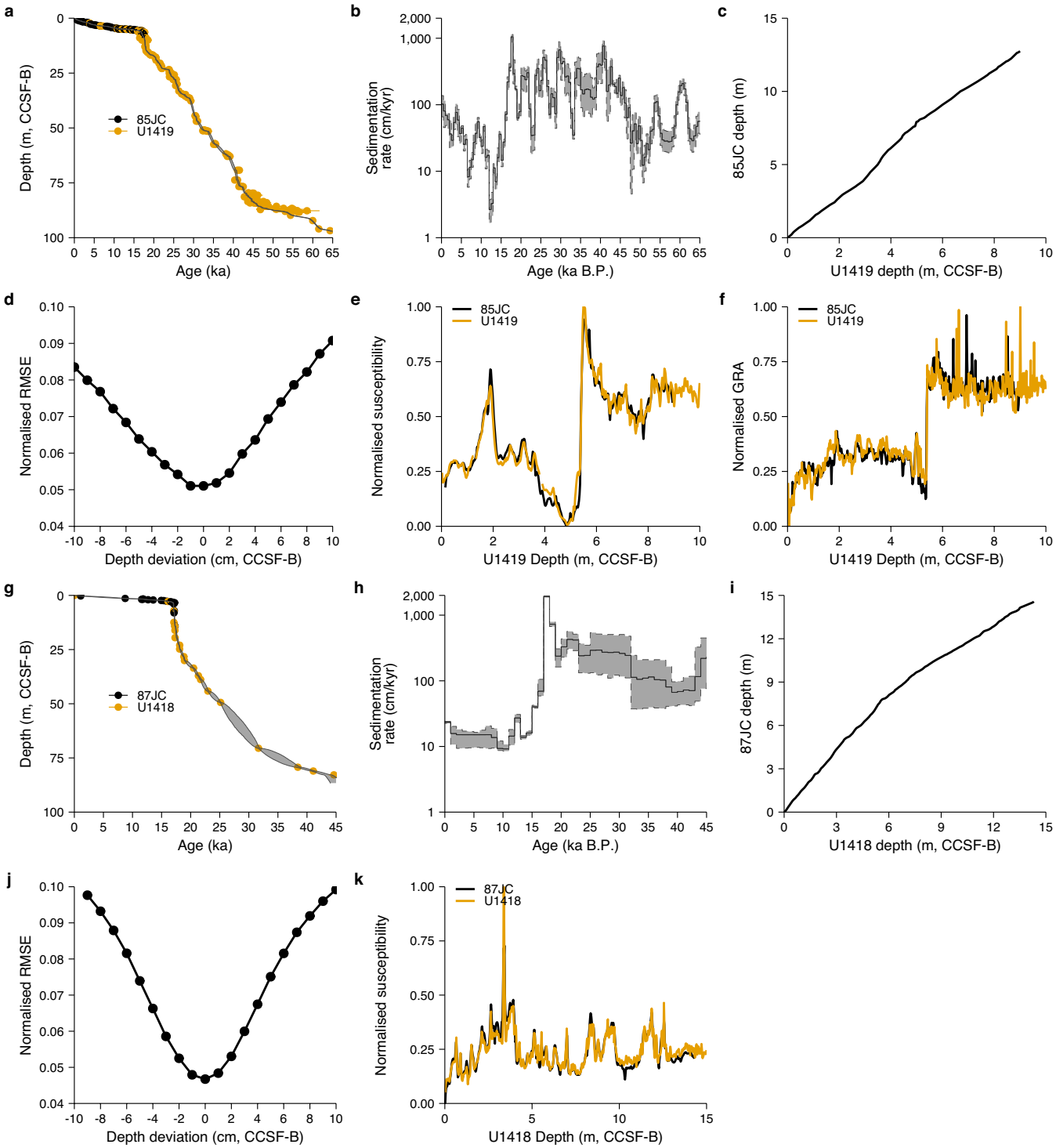

Extended Data Fig. 2 | Bchron[62] Bayesian age models. a–**f**, Age model construction for the intermediate-depth site[4,17]. **a**, Radiocarbon dates (points) calibrated using the Marine20 curve[21] and the modelled depth–age relationship (median line with 1σ range). **b**, Sedimentation rate (median line with 1σ range). **c**, The depth conversion used to align 85JC to U1419. **d**, The normalized and weighted RMSE of GRA and MS misfits as a function of the deviation from the depth conversion in **c**. **e**, Aligned magnetic susceptibility records. **f**, Aligned GRA density records. **g**–**k**, Age model construction for the abyssal site[20]. Only MS was used for alignment in this case. **g**, Radiocarbon dates (points) calibrated using the Marine20 curve[21] and the modelled depth–age relationship (median line with 1σ range). **h**, Sedimentation rate (median line with 1σ range). **i**, The depth conversion used to align 87JC to U1418. **j**, The normalized RMSE of MS misfit as a function of the deviation from the depth conversion in **i**. **k**, Aligned magnetic susceptibility records.

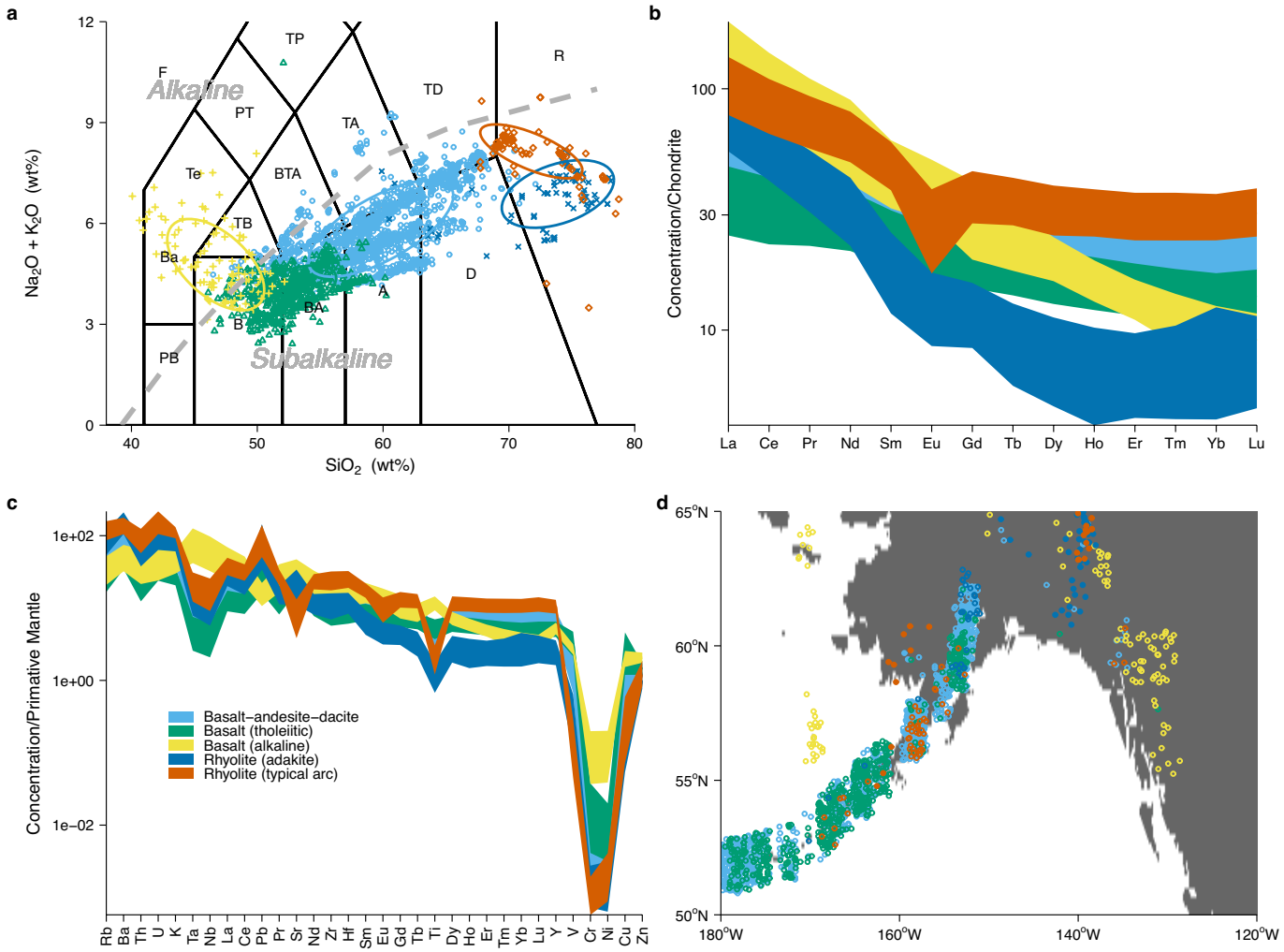

Extended Data Fig. 3 | Geochemistry of the volcanic endmembers identified by cluster analysis. a, Total alkali-silica diagram[127]. Each point represents a sample and the 1σ confidence ellipses of the clusters are shown. **b**, Chondrite[128] normalized REE patterns. **c**, Primitive mantle[128] normalized trace element patterns. The shaded intervals indicate the 1σ ranges (geometric mean and standard deviation) of the endmembers. **d**, Locations of volcanic samples. The location markers are jittered to reduce overlap on the plot. Unfilled circles indicate lava (whole rock) samples. Filled circles indicate tephra (volcanic glass) samples. The locations of the tephra samples are the locations at which they were deposited.

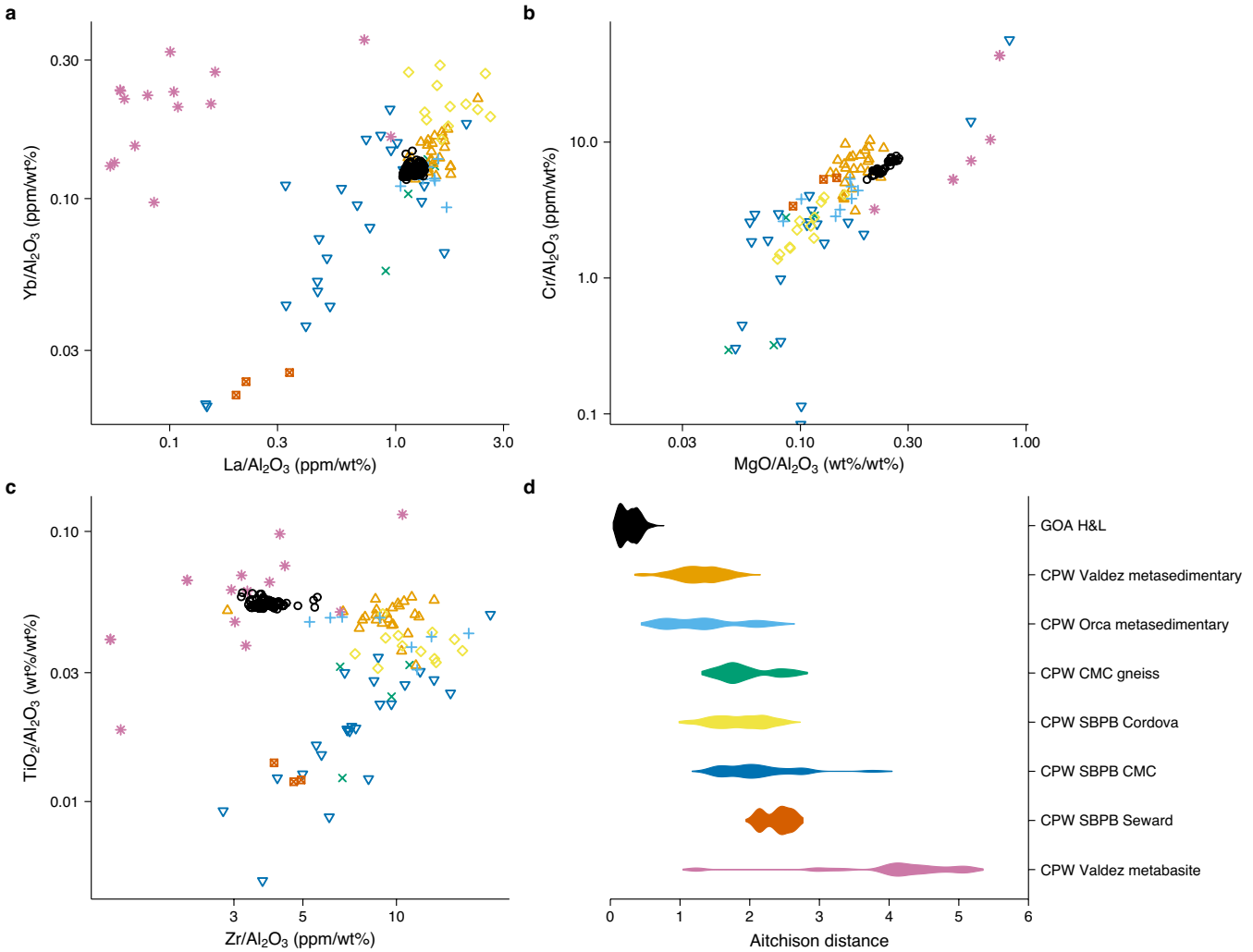

Extended Data Fig. 4 | Geochemistry of the potential terrigenous sediment endmembers compared with sediments at the intermediate-depth site. **a**–**c**, Bi-element plots showing the relationships between GOA Holocene and LGM (H&L) sediments and the terrigenous endmembers[90–96]. **d**, Aitchison distances among the GOA Holocene and LGM sediments, and between them and the terrigenous endmembers[90–96]. Distances are calculated for all possible sample pairs. The *y*-axis is sorted in the order of increasing median distance. The results are summarized using violin plots. The first row in **d** indicates the internal differences among the GOA Holocene and LGM samples, whereas the other rows indicate external differences between the GOA samples and terrigenous endmembers.

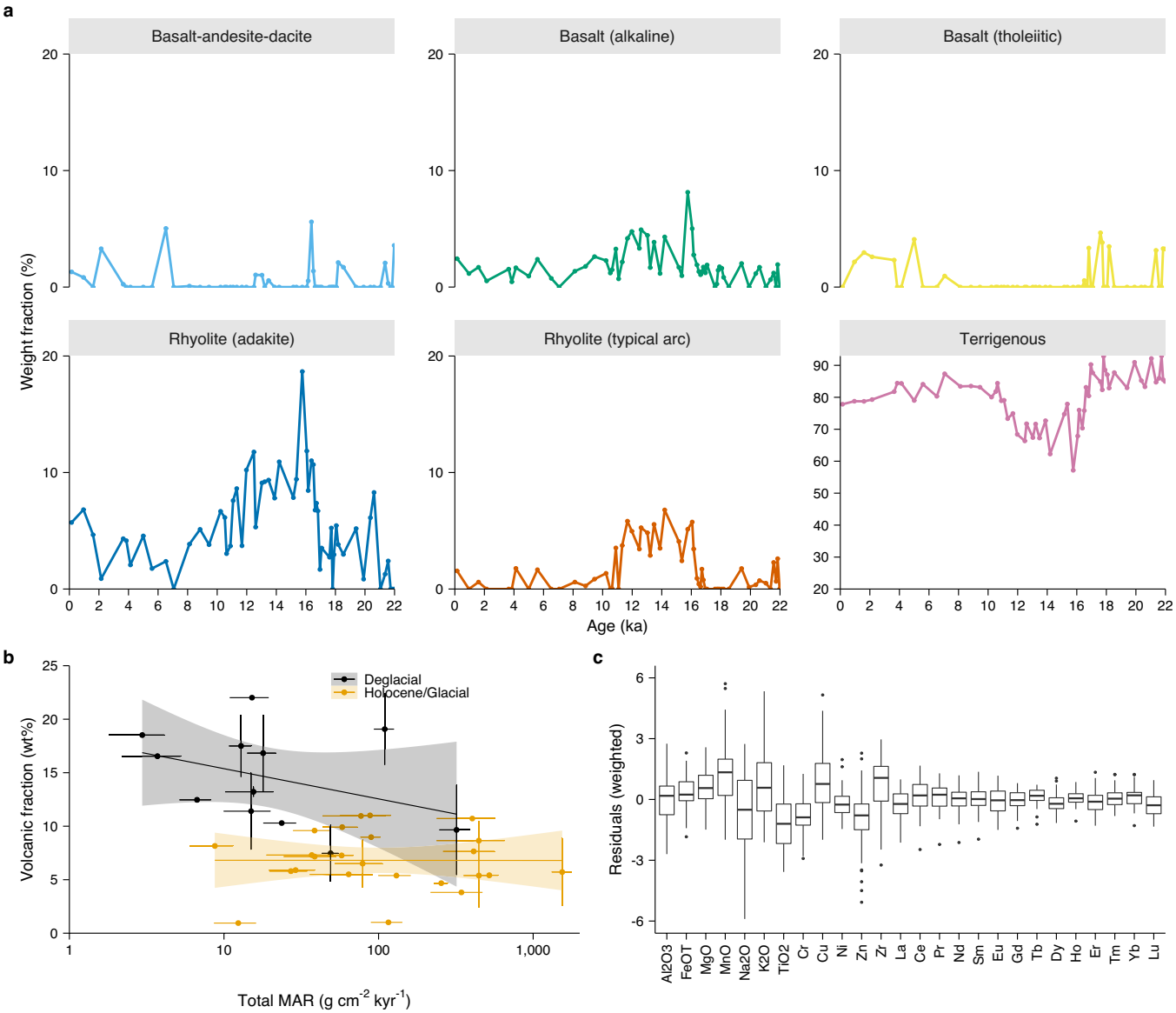

Extended Data Fig. 5 | Geochemical data inversion at the intermediate-depth site. a, Weight fractions of the volcanic endmembers and the terrigenous fractions. **b**, Total volcanic fraction versus total sediment MAR[4]. Lines and shaded intervals (95% CI) indicate linear regression ($P > 0.5$). **c**, Box plots of weighted residuals of the elements in the solution of the geochemical inverse problem. Boxes indicate the interquartile range; thick lines indicate the medians; whiskers extend to 1.5 times the interquartile range away from the boxes.

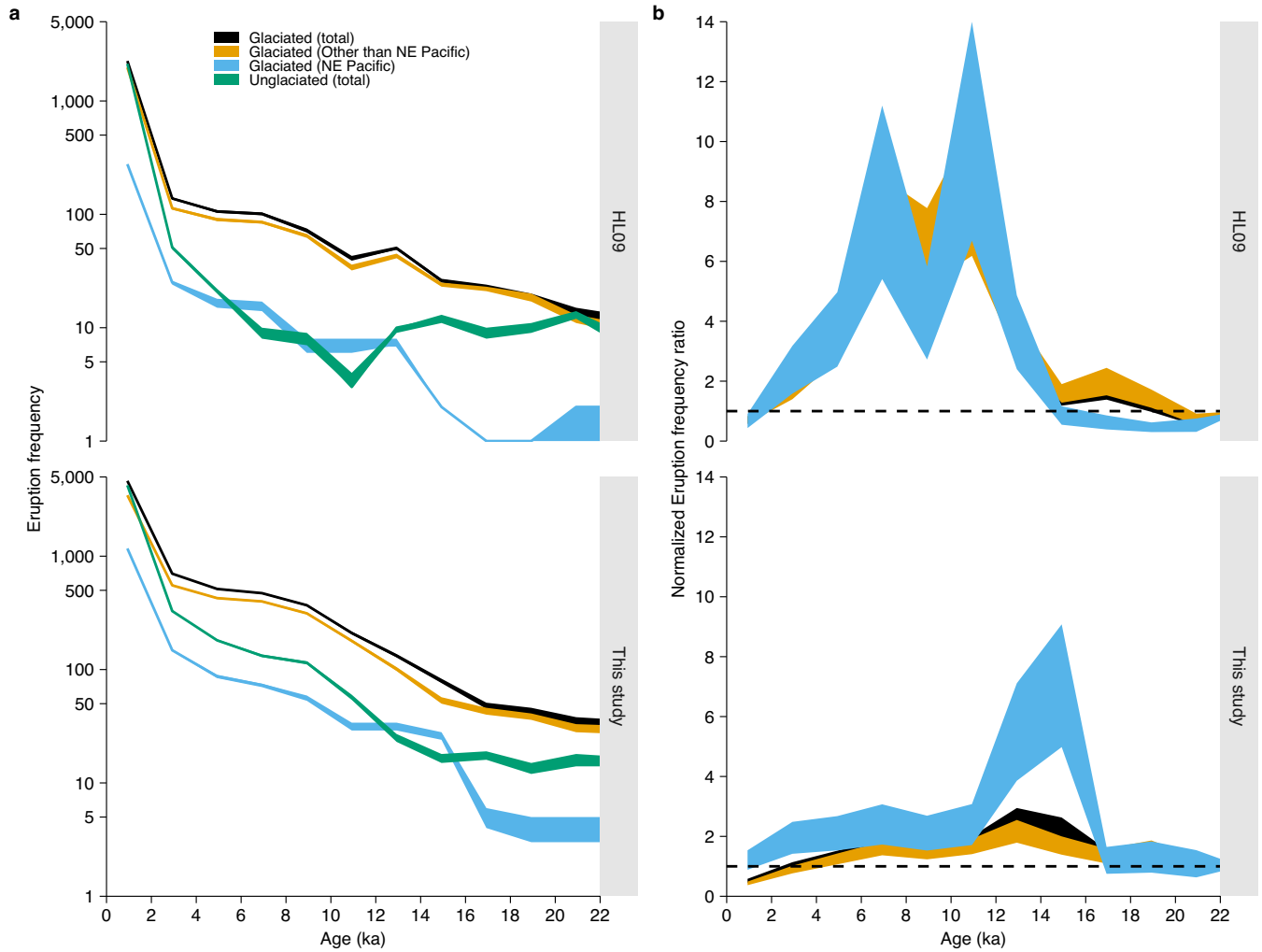

Extended Data Fig. 6 | Records of volcanism since the LGM compiled by this study compared with that of ref. [5]. a, Eruption frequencies of volcanoes binned at 2-kyr intervals. For glaciated volcanoes, the total frequency, as well as the frequency of regional glaciated volcanoes from the Northeast Pacific margin and the rest of the world, are shown. **b**, The ratios of the eruption frequency of the glaciated volcanoes (global total, from the Northeast Pacific margin or elsewhere) to that of the global unglaciated volcanoes, normalized to the mean ratios during the LGM, used as proxies for glacially induced volcanism. The ribbons indicate interquartile ranges. The eruption frequency ratio increases between 12 and 6 ka in Huybers and Langmuir[5], much later than our new compilation (17–11 ka). However, this is because the eruptions of unglaciated volcanoes were under-sampled in Huybers and Langmuir[5] during the deglaciation because their database was smaller (**a**). With greater data coverage, this issue of under-sampling seems resolved in our new compilation.

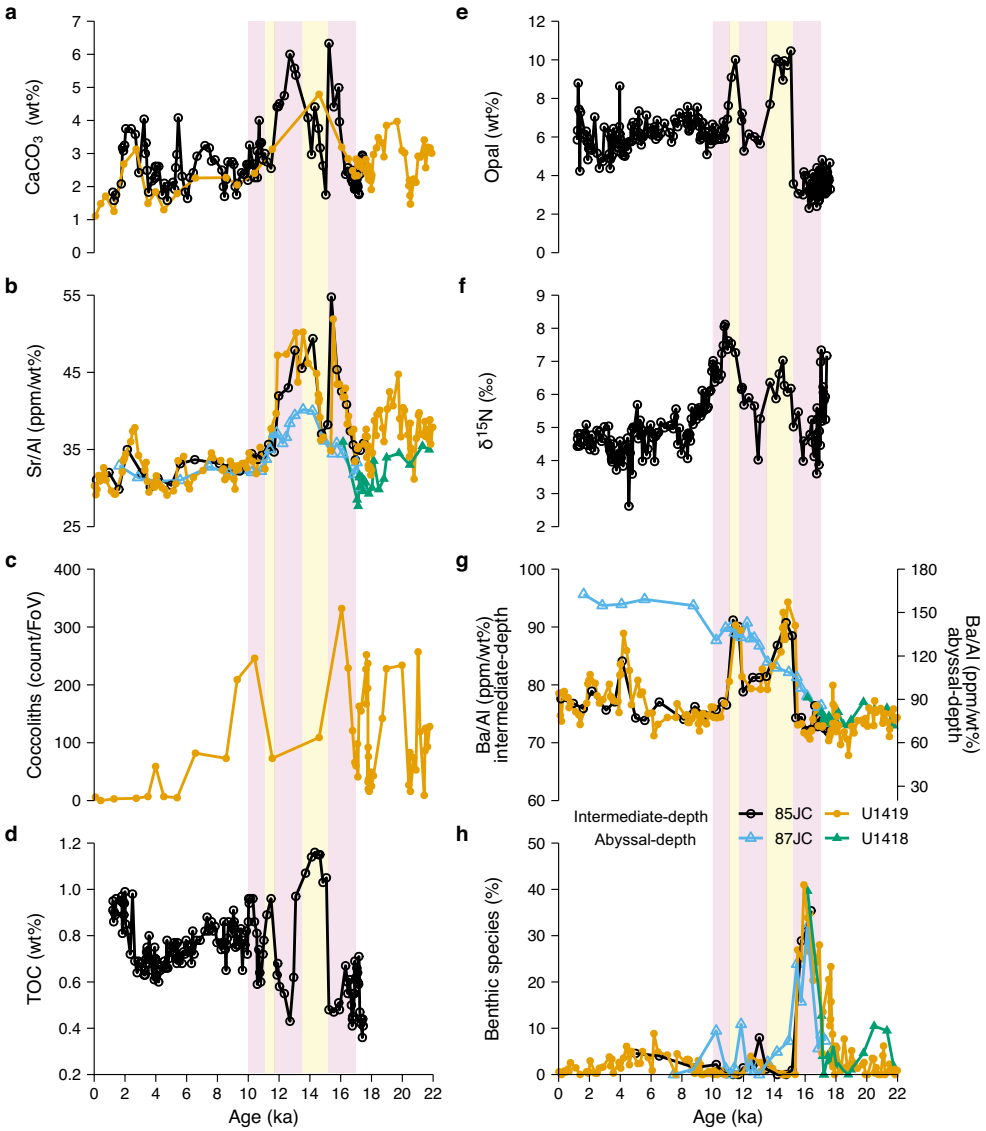

Extended Data Fig. 7 | Northeast Pacific productivity proxies. **a**, $CaCO_3$ content[19,28]. **b**, Sediment Sr/Al ratio. **c**, Counts of coccolith per field of view[19]. **d**, TOC content[28]. **e**, Opal content[28]. **f**, Bulk sediment $\delta^{15}N$, corrected for terrestrial organic matter input[28]. **g**, Sediment Ba/Al ratio. The *y*-axis scales are different between the intermediate-depth and abyssal sites. **h**, Abundances of productivity-related benthic foraminifera species *Islandiella norcrossi* from the intermediate-depth site and *Elphidium batialis* from the abyssal site[12,23]. The colour legends in **a**–**h** are the same.

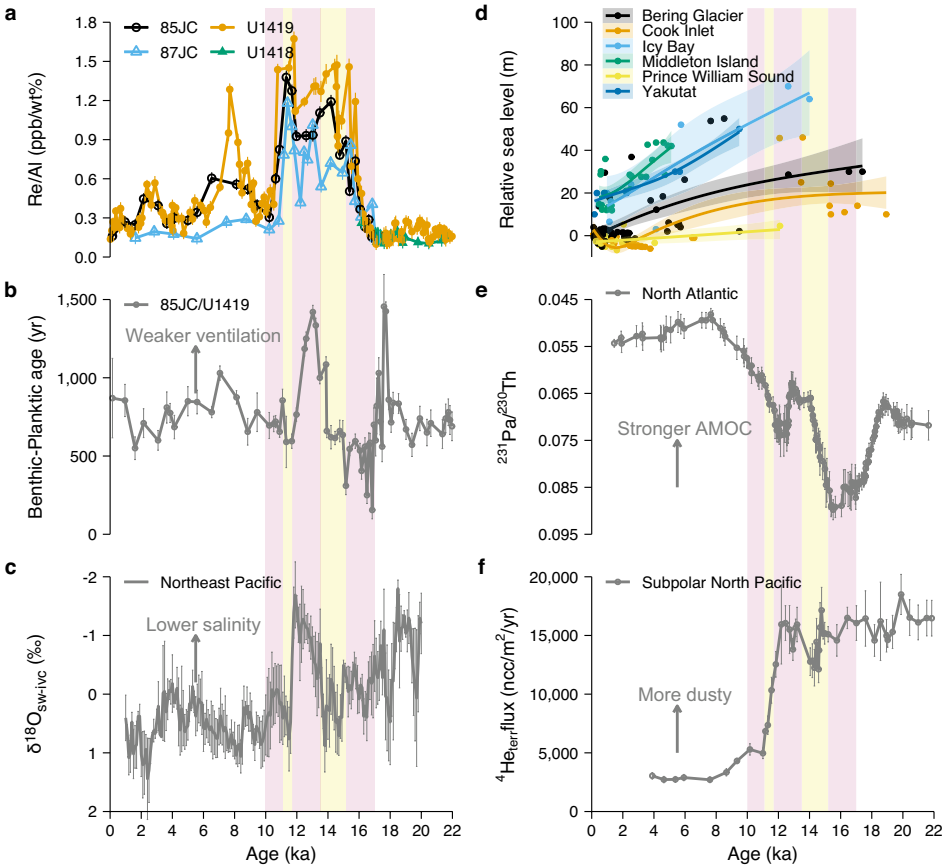

Extended Data Fig. 8 | Records of Northeast Pacific deoxygenation compared with other regional and global climate proxies. a, Re/Al ratios from the GOA sites. **b**, Benthic–planktonic radiocarbon age difference (with 1σ uncertainty) at the intermediate-depth site[4,17], a proxy for intermediate water ventilation. **c**, $\delta^{18}O$ (with 1σ uncertainty) of surface seawater in the Northeast Pacific after removing global ice volume effect[29], a proxy for surface salinity. **d**, Relative sea level in the northern GOA[31] (points with smoothed lines and 95% CI). **e**, $^{231}Pa/^{230}Th$ (with 1σ uncertainty) from the North Atlantic[32], a proxy for the overturning strength of the AMOC. **e**, Terrestrial ^{4}He flux (with 1σ uncertainty) from the subpolar North Pacific[33], a proxy for mineral dust flux that is not affected by volcanic ash input.

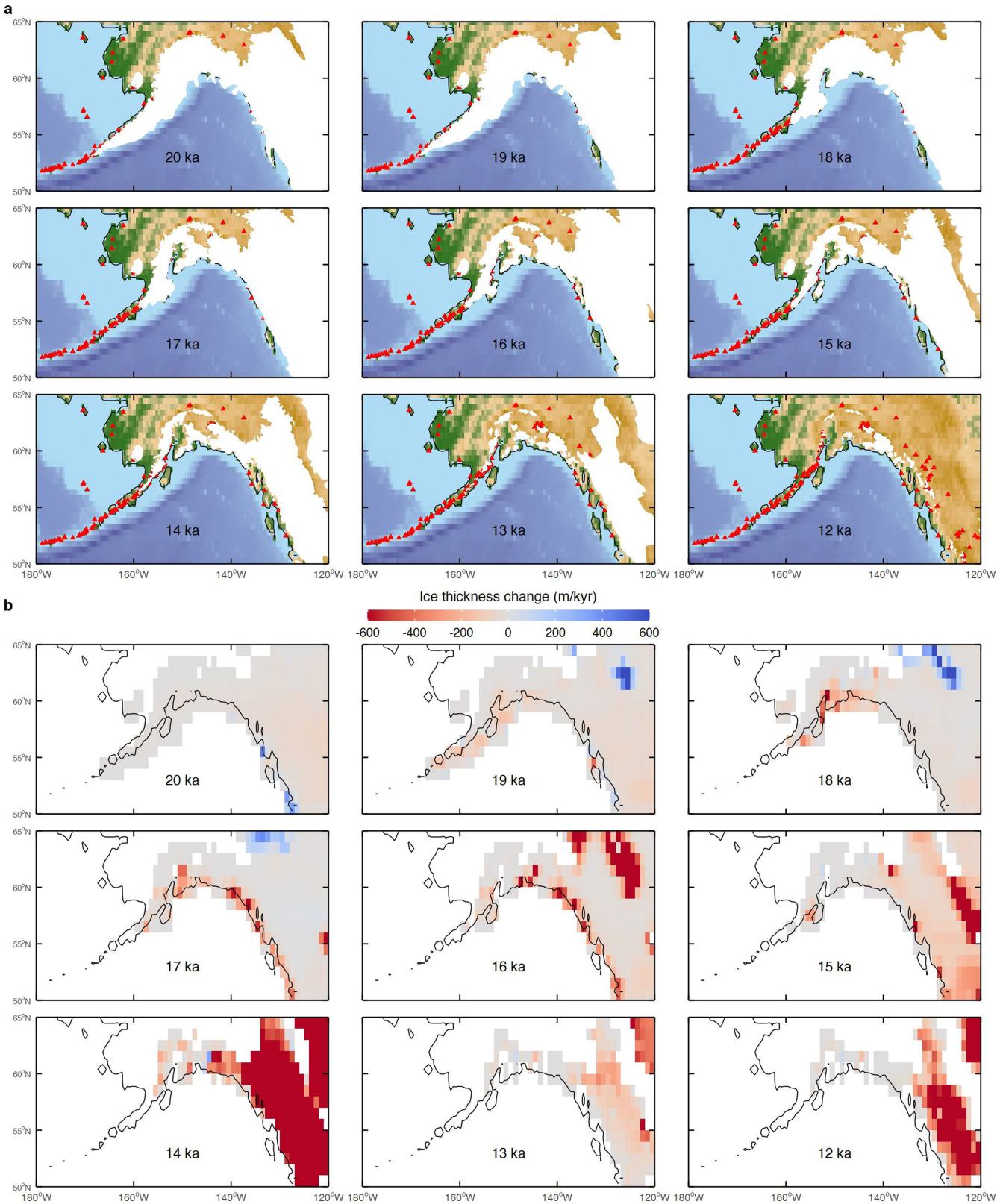

Extended Data Fig. 9 | Histories of the CIS. a, Radiocarbon-based ice sheet extent reconstruction from 20 ka to 12 ka (ref. [41]). **b**, Changes of ice thickness in the ICE-7G model from 20 ka to 12 ka (ref. [25]). Red colour indicates ice loss, whereas blue colour indicates ice accumulation.

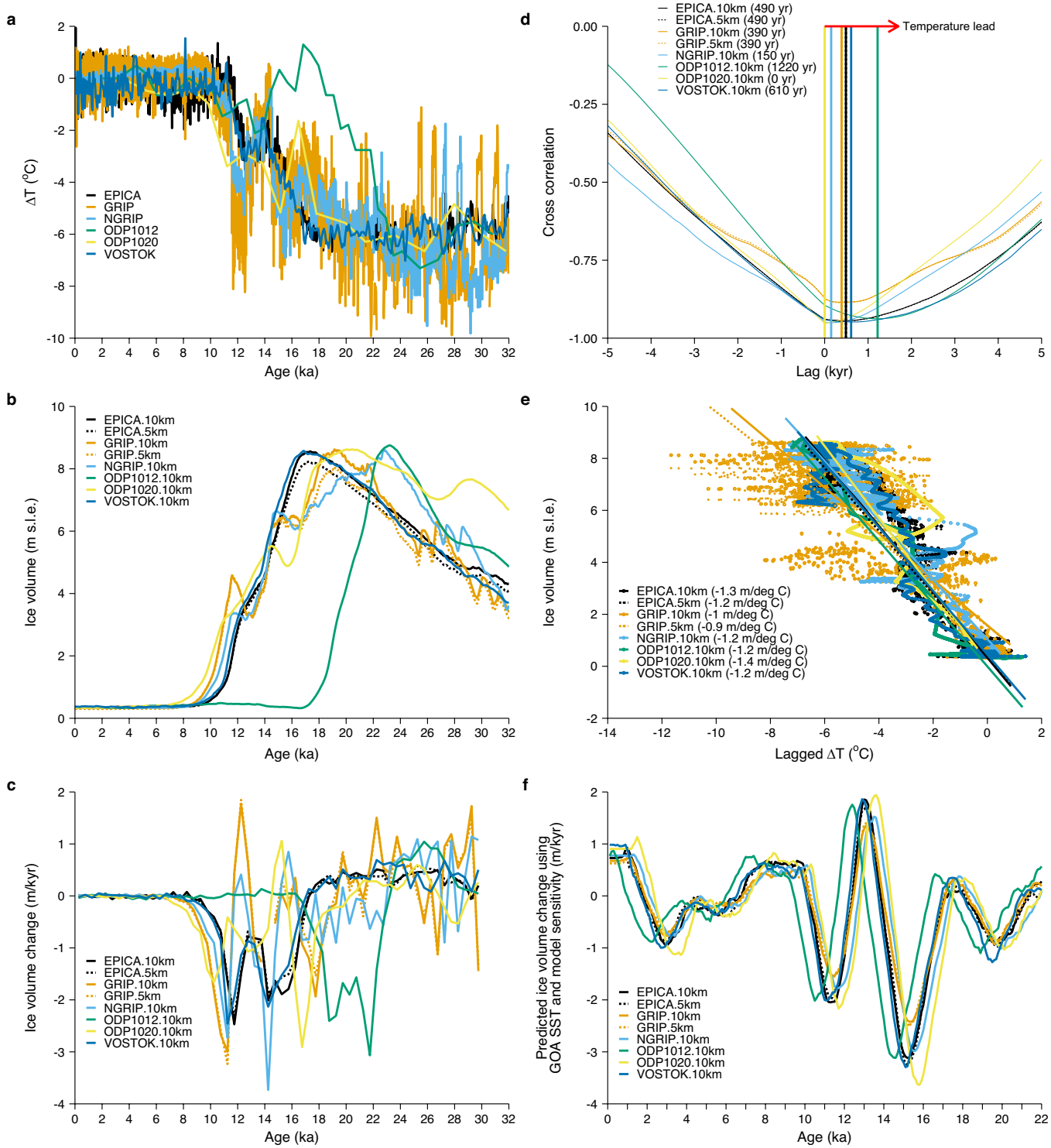

Extended Data Fig. 10 | Sensitivity of the CIS volume to the surface temperature forcing in the PISM model[27]. **a**, Temperature forcing used in the sensitivity experiments (relative to the modern mean) derived from the following temperature records: EPICA[117], GRIP[115], NGRIP[116], VOSTOK[118], ODP 1012 and 1020 (ref. [119]). **b**, Modelled CIS volume in terms of sea-level equivalent. In the EPICA and GRIP experiments, both 5-km and 10-km spatial resolutions were used, whereas in other experiments, only 10-km resolution was used[27]. **c**, Rate of CIS volume change (500-year binned averages). **d**, Lead–lag between the ice volume response and the temperature forcing. Estimated time-lags are indicated by the vertical lines according to the highest negative cross-correlation and the results are shown in the legends inside brackets. **e**, Sensitivity of the CIS volume to the temperature forcing. Linear regression (lines, r^2 between 0.82 and 0.94, $P \ll 0.05$) were performed after shifting the temperature forcing by the time-lags estimated in **c**. Estimated sensitivities in metres of sea-level equivalent per 1 °C are shown in the legends inside brackets. **f**, Predicted rates of CIS volume change (median values) if the GOA SST record is used as the temperature forcing. The results were estimated using the ice volume–temperature relationship in each sensitivity experiment. The final estimate in Fig. 3h incorporates all the sensitivity experiments and uncertainties.